AIAA Aviation
22-26 June 2015, Dallas, TX
22nd AIAA Computational Fluid Dynamics Conference

Development of Vertex–Centered, High-Order Schemes and Implementation in FUN3D

H. Q. Yang[*] *and Robert E. Harris*[†]
CFD Research Corporation
Huntsville, AL

Many production and commercial unstructured CFD codes provide no better than 2nd-order spatial accuracy. Unlike structured grid procedures where there is an implied structured connectivity between neighboring grid points, for unstructured grids it is more difficult to compute higher derivatives due to a lack of explicit connectivity beyond the first neighboring cells. In this study, we have embarked on development of a modular high-order scheme with low dissipation flux difference splitting that can be integrated into existing CFD codes for use in improving the solution accuracy and to enable better prediction of complex physics and noise mechanisms and propagation. The salient features of our approach include: (1) high-resolution schemes with physics-based low-dissipation flux-difference splitting; (2) low memory requirements and small overhead; and (3) modular structure for easy integration into an existing CFD code. Initially, four different aeroacoustic benchmark problems are investigated to assess the accuracy of existing convective schemes in FUN3D. A 3rd-order U-MUSCL scheme using a successive differentiation method is derived and implemented in FUN3D. Verification studies of the acoustic benchmark problems show that the new scheme can achieve up to 4th-order accuracy. Application of the high-order scheme to several acoustic transport and transition-to-turbulence problems demonstrates that with just 10% overhead, the solution accuracy can be dramatically improved by as much as a factor of eight. Studies also demonstrate considerably better agreement with experimental data when using the new 3rd-order U-MUSCL scheme.

I. Introduction

Reducing aircraft noise emissions is an important part of the ongoing efforts to mitigate the impact of commercial aviation on the environment. The anticipated growth of commercial air traffic in the next two decades calls for the development of low-noise aircraft that can offset the projected increase in the community noise exposure. NASA plays a critical role in reducing community noise exposure via technology research and by providing an ambitious noise reduction roadmap for the U.S. aerospace industry. The designations "N+1", "N+2", and "N+3" shown in Figure 1 [1,2], denote three successive aircraft generations for which NASA is conducting research beyond the present generation.

Accurate aircraft airframe and engine noise prediction is crucial for overall aircraft system noise prediction tools. For example, airframe-generated noise is an important component of the total noise radiated from aircraft, especially during aircraft approach and landing when engines operate at reduced thrust, and when airframe components such as high-lift devices, landing gear [3], flaps, and slats are in the deployed state. On the other hand, the noise due to rotor-stator interaction (RSI) is the tonal or broadband noise produced as a result of the interaction between the fan rotor wakes and fan exit guide vanes, and it can be a dominant engine noise source [4].

Detailed understanding of the source mechanisms and subsequent radiation to the far-field is necessary to develop and evaluate noise reduction concepts. Therefore, continued assessment of available prediction tools and development of improved methodologies are essential. Despite significant progress made in the field of computational fluid dynamics (CFD) during the last several decades, prediction of noise sources near complex geometry such as aircraft landing gear is still an extremely challenging problem for the CFD community. The geometric complexity and highly irregular unsteady flow physics associated with landing gear pose numerous difficulties for numerical simulation.

* Chief Scientist, Research, 701 McMillian Way, Huntsville, AL 35806, AIAA Senior Member.
† Senior Principal Engineer, Aeromechanics, 701 McMillian Way, Huntsville, AL 35806, AIAA Senior Member.

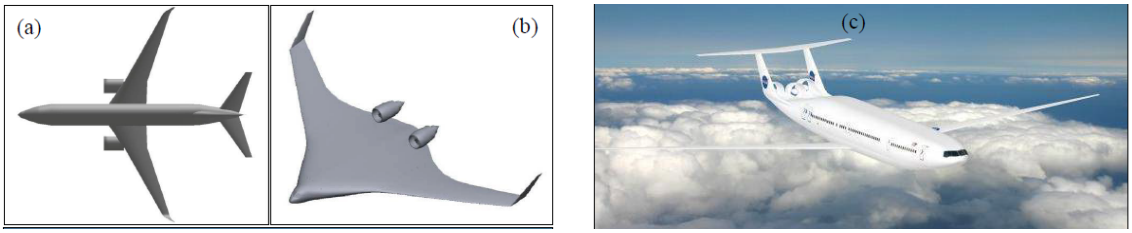

Figure 1. Notional aircraft developed in N+1, N+2, and N+3 studies. (a) N+1 concept aircraft; (b) N+2 concept aircraft; and (c) N+3 concept aircraft, called "double bubble."

The unstructured grid methodology offers significant advantages in terms of grid generation and has been gaining popularity in recent years with increasing emphasis on solving unsteady viscous flow over complex configurations, as evidenced by some recent examples appearing in the literature [5-7]. A representative example from a NASA Langley group led by Dr. Khorrami on aeroacoustic simulation of nose landing gear [3,6-8] is shown in Figure 2.

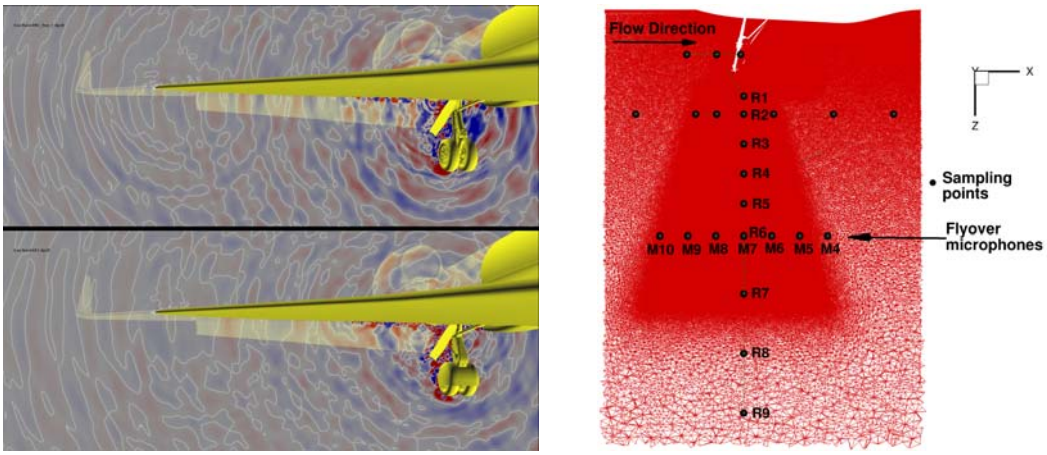

Figure 2. Noise prediction using unstructured CFD Code FUN3D by Khorrami et al. [3,6].

Necessity of High-Order Schemes for Use with Existing Unstructured Grid CFD Codes

Even though the unstructured grid methodology is gaining popularity in the CFD community with increasing emphasis on solving flow over more complex configurations, it is observed that almost all production unstructured CFD codes, such as FUN3D, USM3D, and Loci/CHEM, etc., use 2nd-order spatial schemes. Unlike structured grid procedures where there is an implied structured connectivity between neighboring grid points, for unstructured grids it is more difficult to compute higher derivatives due to a lack of explicit connectivity beyond the first neighboring cells.

CFD simulation of aeroacoustics is focused on the simulation of acoustic fields produced by unsteady flows, and to achieve accurate predictions it is necessary to accurately simulate the evolution of flow disturbances, which requires the use of high-accuracy spatial and temporal numerical schemes. Motivated by the limitation of current production unstructured grid CFD codes to 2nd-order accuracy; the alternative approach of grid adaptation has been undertaken by Vatsa et al. [6]. In this work, it was shown that the correlation from time-averaged and instantaneous solutions to the experimental data improved markedly with grid refinement. Recently, using structured grid CFD combined with high-order finite differencing schemes, Liu et al. [9] showed that both aerodynamic and acoustic results compared well with existing wind tunnel measurement data provided by Airbus for a 1:2.5 scale model of a nose landing gear at a free-stream Mach number of 0.23.

Indeed, high-order schemes can potentially give higher accuracy at lower computational overhead for the simulation of acoustic generation and propagation [10-19]. Since the truncation error of a high-order method decreases more rapidly than that of a lower order method for sufficiently smooth problems, a high-order scheme is more cost effective. With a high-order scheme, CFD has the potential to provide accurate predictions of the acoustic generation, as well as acoustic propagation regions.

Limitation of Existing High-Order Schemes for Unstructured Grid CFD Codes

There has been considerable interest and activities in high-order scheme development for unstructured grids using variants of the discontinuous Galerkin (DG) method [12-18]. In the DG method, one introduces extra degrees-of-freedom (DOFs) in each cell, as shown in Figure 3 to fit a high-order polynomial to the solution. In the sense, a "structured" connectivity is recovered within each cell in the DG method.

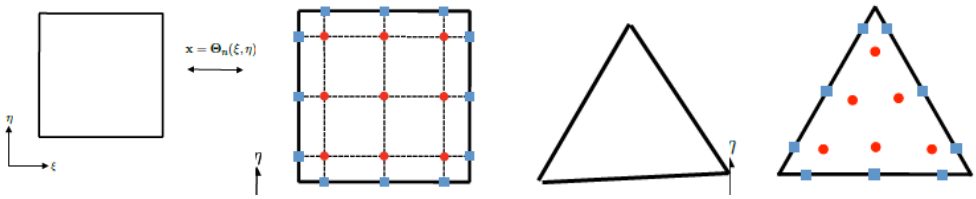

Figure 3. Example stencil for DG scheme for achieving high-order accuracy by adding extra DOFs within each cell.

Table 1 lists the number of required extra DOFs to achieve high-order accuracy when using the DG method. The formulation of DG methods is also very different from the classical finite volume method in that all DOFs within a cell are tightly linked together, and the "mass" matrix is a full matrix (rather than a diagonal matrix), and must be stored and inverted implicitly [17]. As such, the implementation of DG methods into an existing production CFD code requires substantial code modifications. On the other hand, the development of a new production code to take advantage of a new high-order scheme would be prohibitively expensive and require considerable verification and validation efforts.

Table 1. Extra DOFs for high-order schemes using DG.

	p=1, 2nd order	p=2, 3rd order	p=3, 4th order
2D Triangle, (p+1)(p+2)/2	3	6	10
2D Quadrilateral, $(p+1)^2$	4	9	16
3D Tetrahedral, (p+1)(p+2)(p+3)/6	4	10	20
3D Hexahedral, $(p+1)^3$	8	27	64

In this study, we develop an unstructured high-order scheme with low dissipation flux difference splitting that can be integrated into any production unstructured CFD code (such as FUN3D, USM3D, or Loci/CHEM) for noise prediction. The effort builds on our previous work in high-order scheme development for an unstructured pressure-based CFD solver for aeroacoustics [19-21]. In our approach, there is no increase in DOF within each cell. Unlike the k-exact finite volume method, which requires large amounts of extra storage [18], the higher order accuracy in the current approach is achieved by adding higher order correction terms to the governing equations [21]. The present technique is innovative in that it can achieve high-order accuracy without using excessive storage and without introducing extra variables. The high-order method is stable, and can make use of either central or upwind schemes. More importantly, its implementation requires only minor modifications to an existing production CFD code without interfering with the existing code structure and previous validation efforts.

To demonstrate the effectiveness of the proposed high-order schemes in increasing the solution accuracy and resolution, Figure 4 shows results from simulation of a 3D sinusoidal wave propagation problem with the initial condition and error convergence rate for several different high-order schemes that have been developed [21]. The equivalent cell size is represented by the cube root of the total DOFs. For the hexahedral grid, the present 2nd-order central and upwind schemes all show a 2nd-order convergence rate as expected. The 3rd-order upwind scheme has lower error than the 2nd-order schemes and actually exhibits a 3rd-order convergence rate. The 4th-order upwind and the 3rd-order central schemes all display a 4th-order convergence rate, and the 4th-order central scheme has the lowest error and a 5th-order convergence rate.

Previous studies have suggested that a 2nd-order scheme requires at least 16 points per wavelength to accurately resolve the wave propagation. As illustrated by the dotted line in Figure 4, one needs only 6 points per wavelength using the 4th-order central scheme to achieve the same L_2 error. The savings in the total cell count is a factor of 19 for this 3D problem. Our experience with the pressure-based solver indicates that with an overhead of around 50% on CPU, the grid resolution can be increased by one order-of-magnitude (10X). In other words, a 4th-order solution using this scheme on a grid comprised of 1

billion cells can provide a resolution equivalent to that from a 2nd-order scheme using 10 billion cells. Table 2 also lists the equivalent cell count per wavelength for different high-order schemes and the savings in the total cell count.

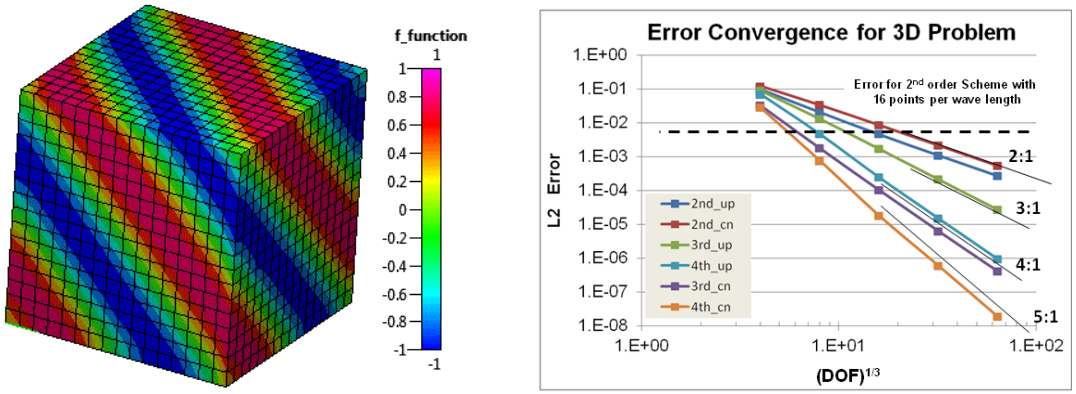

Figure 4. Initial condition (left) and error convergence rate (right) for the present high-order scheme using the pressure-based unstructured grid CFD solver, CoBi.

Table 2. Equivalent points per wavelength and total saving for the same L_2 error.

Schemes	2nd Order Upwind	3rd Order Upwind	3rd Order Central	4th Order Upwind	4th Order Central
Order of Accuracy	2	3	4	4	5
Points Per Wavelength	16	12	7	8	6
Total Cell Number Saving	1X	2.37X	11.9X	8X	19X

II. FUN3D CFD Code

Our experience with the initial development of the proposed high-order scheme was with the pressure-based CFD solver, CoBi [19-21]. In the current study, a generic 3rd-order interpolation module is developed for a density-based, unstructured CFD code, and the module is integrated into the NASA unstructured CFD code, FUN3D [22]. The accuracy of the new scheme with respect to the designed accuracy is evaluated for several acoustic wave propagation problems. Prior to integrating our high-order module into FUN3D, it is important to understand the code structure and accuracy of the existing 2nd-order schemes in FUN3D.

FUN3D is an unstructured grid flow solver developed originally by Anderson and Bonhaus [23], and the code has gone through significant modifications over the years by a team of researchers at NASA Langley using modern software practices [24]. The discrete form of the governing equations is solved either in a time-accurate manner with a constant time step at every grid point or with variable time stepping to accelerate convergence to a steady state. At each iteration step, the linear system of equations is relaxed in a red-black fashion with a point implicit procedure [24]. The FUN3D code can accommodate multiple grid types including tetrahedra, prisms, pyramids and hexahedra, which makes it compatible with many different grid generation packages.

In FUN3D, the flow variables are stored at the vertices or nodes of the mesh, and the inviscid fluxes are computed at interfaces between neighboring control volumes surrounding each node using an approximate Riemann solver based on the values on either side of the interface. Several convective flux schemes are available, and the most common scheme for subsonic and transonic flows is Roe's flux difference splitting [25]. For 2nd-order accuracy, interface values are obtained by extrapolation of the mesh vertex values based on gradients computed using an unweighted least-squares technique, and several reconstruction limiters are available to maintain stability in the presence of shocks and discontinuities.

Governing Equations

The governing equations solved in FUN3D are the time-dependent Reynolds-averaged Navier-Stokes (RANS) equations. The equations are expressed as a system of conservation laws that relate the time rate-of-change of mass, momentum, and energy

in a control volume to the spatial fluxes of these quantities through the volume. The equations (nondimensionalized by free-stream density, speed of sound, temperature, viscosity, thermal conductivity, and a reference length) are given as:

$$\Omega \frac{\partial Q}{\partial t} + \oint_{\Omega} \vec{F}_i \bullet \hat{n} dl - \oint_{\Omega} \vec{F}_v \bullet \hat{n} dl = 0, \tag{1}$$

where $\hat{n}$ is the outward-pointing unit normal to the control volume, $\vec{F}_i$ is the inviscid flux vector, and $\vec{F}_v$ is the diffusive flux vector. The vector of dependent variables Q, and the inviscid and viscous flux vectors in 2D are:

$$Q = \begin{Bmatrix} \rho \\ \rho u \\ \rho v \\ \rho E \end{Bmatrix}, \tag{2}$$

$$\vec{F}_i = f\hat{i} + g\hat{j} = \begin{Bmatrix} \rho u \\ \rho u^2 + p \\ \rho uv \\ (E+p)u \end{Bmatrix} \hat{i} + \begin{Bmatrix} \rho v \\ \rho uv \\ \rho v^2 + p \\ (E+p)v \end{Bmatrix} \hat{j}, \tag{3}$$

and

$$\vec{F}_v = f_v\hat{i} + g_v\hat{j} = \begin{Bmatrix} 0 \\ \tau_{xx} \\ \tau_{xy} \\ u\tau_{xx} + v\tau_{xy} - q_x \end{Bmatrix} \hat{i} + \begin{Bmatrix} 0 \\ \tau_{xy} \\ \tau_{yy} \\ u\tau_{xy} + v\tau_{yy} - q_y \end{Bmatrix} \hat{j}. \tag{4}$$

The shear stress and heat conduction terms are given as

$$\begin{aligned} \tau_{xx} &= (\mu + \mu_t) \frac{M_\infty}{\mathrm{Re}} \frac{2}{3} (2u_x - v_y) \\ \tau_{yy} &= (\mu + \mu_t) \frac{M_\infty}{\mathrm{Re}} \frac{2}{3} (2v_y - u_x) \\ \tau_{xy} &= \tau_{yx} = (\mu + \mu_t) \frac{M_\infty}{\mathrm{Re}} \frac{2}{3} (u_y + v_x). \\ q_x &= -\frac{M_\infty}{\mathrm{Re}(\gamma - 1)} \left(\frac{\mu}{\mathrm{Pr}} + \frac{\mu_t}{\mathrm{Pr}_t} \right) \frac{\partial T}{\partial x} \\ q_y &= -\frac{M\infty}{\mathrm{Re}(\gamma - 1)} \left(\frac{\mu}{\mathrm{Pr}} + \frac{\mu_t}{\mathrm{Pr}_t} \right) \frac{\partial T}{\partial y} \end{aligned} \tag{5}$$

The equations are closed with the equation of state for a perfect gas

$$\mu = \frac{\bar{\mu}}{\bar{\mu}_\infty} = \frac{(1+C^*)(T/T_\infty)^{3/2}}{T/T_\infty + C^*}, \tag{6}$$

where C* =198.6/460.0 is Sutherland's constant divided by a free-stream reference temperature, which is assumed to be 460° R.

Discretization

FUN3D employs vertex-centered implicit finite-volume schemes [23]. In this approach, the computational domain is divided into a finite number of cells from which control volumes are formed that surround each vertex in the mesh. The flow variables are stored at each mesh vertex. Equation (1) is then numerically integrated over the closed boundaries of the control volumes surrounding each vertex. These control volumes are formed by connecting the center of each cell to the midpoint of the cell edges, as shown in Figure 5. These nonoverlapping control volumes are constructed to completely cover the domain and are considered to form a mesh which is dual to the original mesh composed of cells formed from the vertices.

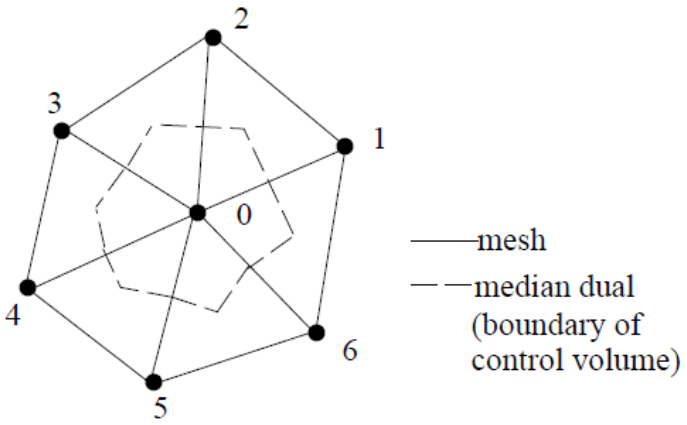

Figure 5. Control volume surrounding a node.

The numerical evaluation of the surface integrals in Equation (1) is conducted separately for the inviscid and viscous contributions. For a finite-volume formulation, the inviscid contribution can be approximated using midpoint integration of the fluxes over each edge of the dual mesh that defines the boundary of the control volume. i.e.

$$\oint \vec{F} \bullet \hat{n} dl = \oint \vec{F} \bullet d\hat{n} = \sum_{i=1} \Phi(Q_i^+, Q_i^-; \hat{n}_i) l_i \,. \tag{7}$$

The above integration is over all edges of the dual mesh that make up the surface of the control volume and *l* is the length of the edge. Also, $\Phi(Q^+, Q^-; \hat{n})$ is a numerical flux formed from data on the left (Q^+) and right sides (Q^-) of the face which are determined by interpolation from the surrounding data. The flux calculations for a node are made by distributing the contributions from each of the edges.

To obtain an upwind scheme, the numerical fluxes on the edges of the control volume are computed using Roe's approximate Riemann solver [25]. These fluxes are formed from data on either side of the face as

$$\Phi = \frac{1}{2}\left(\vec{F}(Q^+, \hat{n}) + \vec{F}(Q^-, \hat{n})\right) - \frac{1}{2}\left|A(Q, \hat{n})\right|(Q^+ - Q^-) \,. \tag{8}$$

As was discussed earlier, the variables are known at the vertices while the fluxes are needed at the cell faces. For conventional 2nd-order schemes, the reconstruction step is expressed as:

$$Q_f = Q_P + \psi \nabla Q \bullet (\mathbf{r}_f - \mathbf{r}_P) \,, \tag{9}$$

where ψ is a limiter function in order to avoid numerical oscillations in the regions of steep gradients. Two examples of such limiter functions are the Barth limiter [26] and the Venkatakrishnan limiter [27]. At interface *e*, the 2nd-order scheme can be expressed as:

$$Q_e^{+} = Q_P + \psi(\nabla Q)_P \bullet (\mathbf{r}_e - \mathbf{r}_P), \tag{10}$$

$$Q_e^{-} = Q_E + \psi(\nabla Q)_E \bullet (\mathbf{r}_e - \mathbf{r}_E). \tag{11}$$

Least Squares Method

For evaluating the gradient, ∇Q, FUN3D uses a least squares procedure in which the data surrounding each node is assumed to behave linearly. Referring to Figure 6 as an example, the data at each node surrounding the center node may be expressed as

$$Q_i = Q_0 + \frac{\partial Q}{\partial x}(x_i - x_0) + \frac{\partial Q}{\partial y}(y_i - y_0). \tag{12}$$

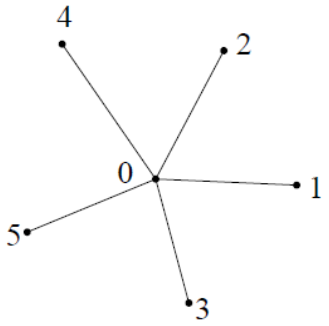

Figure 6. Nodes for least squares reconstruction of data.

By expressing the data in a like manner at each of the N surrounding nodes, an Nx2 system of equations is formed which can be solved to obtain the gradients at the nodes

$$\begin{bmatrix} \Delta x_1 & \Delta y_1 \\ \Delta x_2 & \Delta y_2 \\ . & . \\ . & . \\ \Delta x_N & \Delta y_N \end{bmatrix} \begin{Bmatrix} \frac{\partial Q}{\partial x} \\ \frac{\partial Q}{\partial y} \end{Bmatrix} = \begin{Bmatrix} Q_1 - Q_0 \\ Q_2 - Q_0 \\ . \\ . \\ Q_N - Q_0 \end{Bmatrix}. \tag{13}$$

This represents an over-determined system of linear equations, $A\mathrm{x} = b$, which may be solved using a least squares approach. In FUN3D, a Gram-Schmidt process is used in which the system of equations is solved by decomposing the A matrix into a product of an orthogonal matrix Q, and an upper triangular matrix R, i.e.

$$A = QR, \tag{14}$$

so that the solution is obtained by:

$$x = R^{-1}Q^T b. \tag{15}$$

U-MUSCL Scheme

A variable extrapolation formulation for unstructured finite volume codes developed by Burg [28] has been implemented in FUN3D. This scheme is called U-MUSCL and closely resembles the MUSCL scheme used within structured flow solvers. The formulation is based on information currently available to the unstructured flow solvers, namely the solution and gradient information, and as such, it is trivial to implement within most finite-volume flow solvers. In the U-MUSCL scheme, the interpolation function in Equation (9) is replaced by:

$$Q_L(\kappa) = Q_i + \psi\left[\frac{\kappa}{2}\left(Q_j - Q_i\right) + \left(1-\kappa\right)\nabla Q_i \bullet \vec{r}_{ij}\right], \tag{16}$$

where κ is the U-MUSCL parameter, and Q_i and Q_j are the flow variables at the nodes on the either side of the face. This new variable extrapolation formulation represents a one-parameter family of schemes. Under certain circumstances, it is fully equivalent to the MUSCL-scheme, which is also a one-parameter family. In one-dimension, if the central difference approximation is used for the gradient (i.e., $\nabla Q = (Q_{i+1} - Q_{i-1})/(2h)$) then this scheme reduces to the MUSCL scheme.

Table 3 shows the multiple different schemes that can arise based on the choice of parameter κ. If κ is set to 0, then the original unstructured formulation for 2nd-order variable extrapolation is obtained. If κ is set to -1, then the 2nd-order fully upwind MUSCL-type variable extrapolation is obtained. If κ is set to 1/2, a 3rd-order variable extrapolation to the cell face is achieved, while if κ is set to 1/3, a 3rd-order approximation to the derivative at the node is achieved. When κ is set to 1, a central difference scheme is obtained. This formula is an upwind formula as long as $\kappa < 1$ and as such is stable for hyperbolic systems of equations that do not contain shocks and for high-quality grids.

Table 3. U-MUSCL Scheme with Different Parameter κ Values.

κ	Comments
-1	2nd-Order MUSCL-type Scheme
0	2nd-Order Unstructured Upwind Scheme
1/3	3rd-Order MUSCL-type Scheme
1/2	3rd-Order Extrapolation to Face
1	Central Difference Formula

III. Evaluation of Existing Schemes in FUN3D

Solution of 1D Acoustic Propagation

Prior to implementing high-order schemes into FUN3D, it is important to assess the accuracy of existing schemes in FUN3D for later use in verifying improvements to the code. Let us consider the case where there is a uniform flow. Let:

$$\rho = \rho_\infty + \rho'; \quad u = u_\infty + u'; \quad p = p_\infty + p', \tag{17}$$

where the subscript "∞" denotes the uniform, mean flow and the prime denotes fluctuations about the mean flow. The continuity, momentum and energy equations can be transformed to:

$$\begin{aligned} \frac{\partial \rho'}{\partial \tau} &= -\rho_\infty \frac{\partial u'}{\partial x'} \\ \frac{\partial u'}{\partial \tau} &= -\frac{1}{\rho_\infty}\frac{\partial p'}{\partial x'} \\ \frac{\partial p'}{\partial \tau} &= -\frac{1}{M_\infty{}^2}\frac{\partial u'}{\partial x'} \\ x' &= x - u_\infty t; \quad \tau = t \end{aligned} \tag{18}$$

The following analytical solution exists for the above equations:

$$p'(x,t) = A_1 e^{ik[x-(u_0-\frac{u_0}{M_0})t]} + A_2 e^{ik[x-(u_0+\frac{u_0}{M_0})t]}, \tag{19}$$

$$u'(x,t) = \frac{M_0}{\rho_0 u_0}\left(A_1 e^{ik[x-(u_0-\frac{u_0}{M_0})t]} + A_2 e^{ik[x-(u_0+\frac{u_0}{M_0})t]} \right), \tag{20}$$

where A_1 and A_2 are determined from the initial condition. Using the non-dimensionalization employed in FUN3D, the initial condition is specified as:

$$\begin{aligned} p(x,0) &= p_\infty + A * \cos[2\pi k x] \\ u(x,0) &= u_\infty + \frac{k}{\rho_\infty c_\infty} A \sin[2\pi k x] \end{aligned} \tag{21}$$

The solution to Equations (19,20) with the initial conditions (21) is:

$$\begin{aligned} p(x,t) &= p_\infty + A * \cos[2\pi k(x - M_\infty t)] * \cos[2\pi k t] \\ u(x,t) &= u_\infty + \frac{k}{\rho_\infty c_\infty} A * \sin[2\pi k(x - M_\infty t)] * \sin[2\pi k t] \end{aligned} \tag{22}$$

In this study, we set M_∞=0.2, A=1.0x10^{-5} and k=1. As shown in Figure 7, the computational domain has a non-dimensional length of 1 with periodic boundary conditions in the x-direction. The boundaries in the y and z directions have a zero gradient condition. We employ a series of increasingly fine grids with 8, 16, 32, 64 and 128 cells in the x direction to investigate the convergence rate and spatial accuracy of the FUN3D schemes. The 2nd– and 3rd-order temporal schemes are selected, and the time step sizes are selected such that the solution is time-step independent.

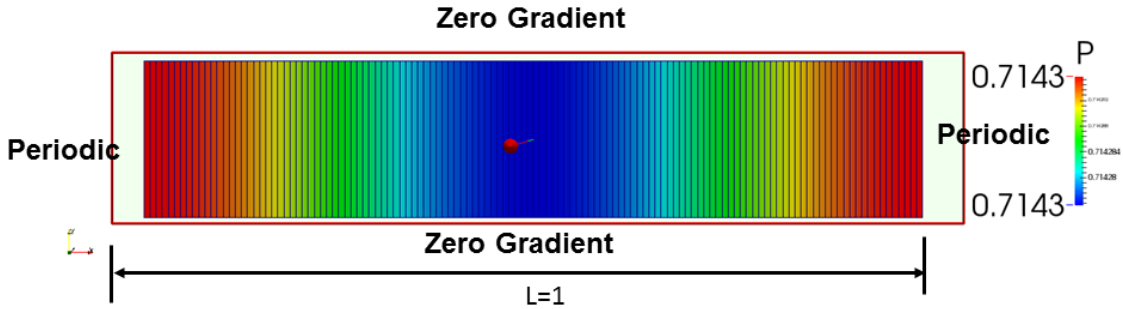

Figure 7. Computational model for 1D acoustic problem.

Figure 8 shows the analytical solution of the above problem when M_∞=0, as well as the pressure variation with time at the center of the domain which displays a sinusoidal functional form with constant amplitude. With zero freestream Mach number, the solution is a standing wave, and with non-zero Mach number, it is a traveling wave.

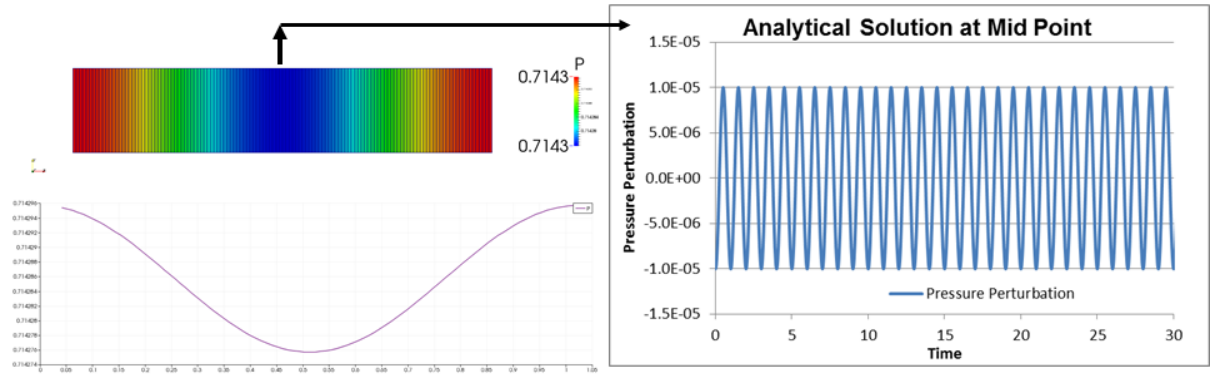

Figure 8. The analytical solution to the 1D acoustic problem.

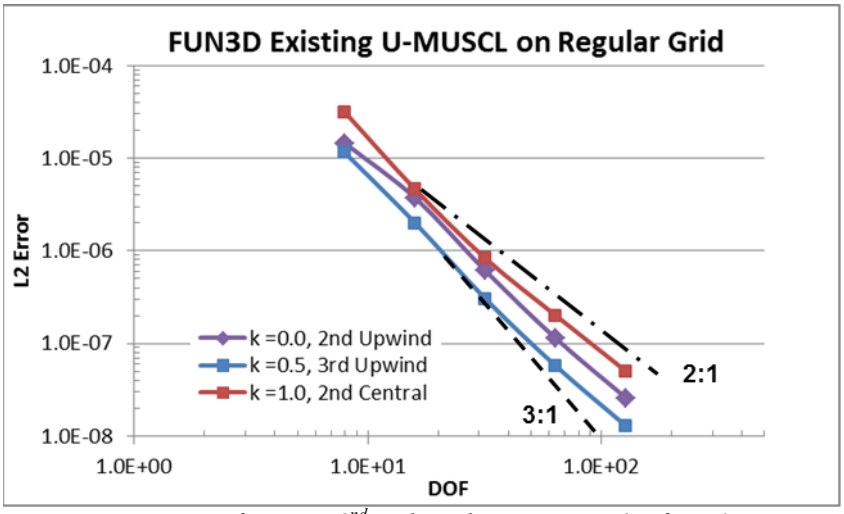

Figure 9. Error convergence of existing 2nd-order schemes in FUN3D for a 1D acoustic problem.

The error convergence rate under grid refinement for three different values of the U-MUSCL parameter κ is shown in Figure 9. For κ=0, it is equivalent to the standard 2nd-order upwind scheme as used in typical unstructured grid solvers. No limiter is applied in this case. When κ=0.5, this is the 3rd-order upwind scheme as described by Burg [28], and when κ=1, it is a central difference scheme where the face value is simply the average of the two nodes. As one can see, results for both 2nd-order upwind and 2nd-order central schemes exhibit 2nd-order convergence rates, with the central scheme resulting in larger errors than the upwind scheme. On the other hand, when κ=0.5, the solution indeed gives a lower error in comparison to other values of κ=0 or κ=1. However, the convergence rate is not truly 3rd-order.

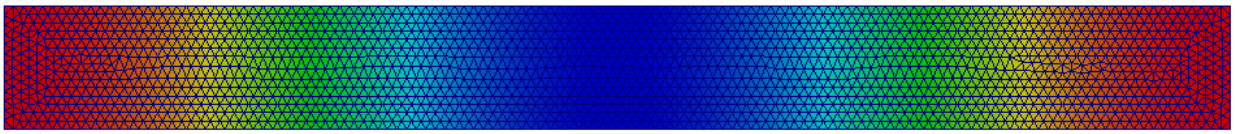

Figure 10. Computational unstructured grid for 1D acoustic problem.

The above 1D acoustic problem is now revisited using an unstructured grid comprised of similar length scales. An example grid used for this study is shown in Figure 10, and Figure 11 shows the convergence of the U-MUSCL scheme on the unstructured grid. As expected, the central scheme becomes unstable with increasing grid resolution. On the other hand, the 2nd-order and 3rd-order upwind schemes show the same convergence rate, which is higher than 2nd-order and lower than 3rd-order. The mean convergence rate is 2.35. One also notices that it is beneficial to use the U-MUSCL scheme with κ=0.5 as default since it gives a lower error.

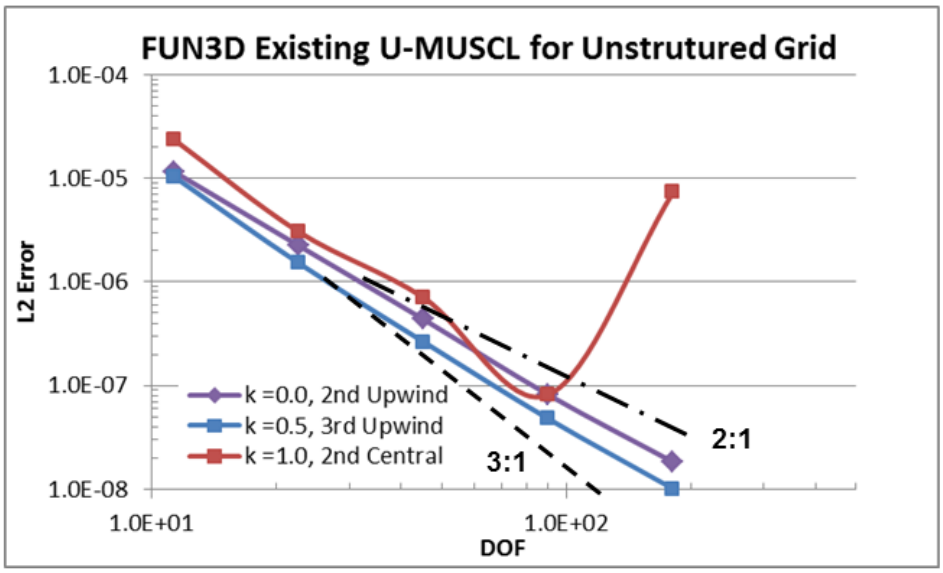

Figure 11. Error convergence of existing 2nd-order schemes in FUN3D for 1D acoustic problem.

Solution of 2D Vortex Transport Problem

We now consider the verification of the upwind scheme in FUN3D for a 2D compressible flow problem. We will study the transport of a vortex in a compressible fluid as the test case since there is a well-known analytical solution available. The ability to conserve the vortex shape and strength is necessary for aeroacoustics since there are many practical scenarios in which a shed vortex interacts with bodies well downstream of the vortex source to generate sound. The present inviscid vortex transport study examines the relative dissipation and dispersion errors for the inviscid flux schemes. The computational domain has a size of $(x,y)=(-L_x,L_x)\ (-L_y,L_y)$, and the flowfield is initialized as:

$$
\begin{aligned}
u &= u_\infty - \beta u_\infty \frac{y-y_c}{R}\exp\left(\frac{1-r^2}{2}\right) \\
v &= v_\infty + \beta u_\infty \frac{x-x_c}{R}\exp\left(\frac{1-r^2}{2}\right) \\
\rho &= \rho_\infty\left[1-\frac{\gamma-1}{2\gamma}(\beta u_\infty)^2\exp(1-r^2)\right]^{\frac{1}{\gamma-1}} \\
p &= p_\infty\left[1-\frac{\gamma-1}{2\gamma}(\beta u_\infty)^2\exp(1-r^2)\right]^{\frac{\gamma}{\gamma-1}}
\end{aligned}
\tag{23}
$$

where $r=\sqrt{(x-x_c)^2+(y-y_c)^2}\,/\,R$, $\beta=1/2\pi$, $x_c=y_c=0$, $u_\infty=0.2$, $v_\infty=0$, $R=0.01$, and $L_x=L_y=0.05$. The computational model for the regular and unstructured grids is shown in Figure 12 along with the initial pressure field.

The error convergence rates for this 2D vortex transport problem using the U-MUSCL scheme in FUN3D on the regular structured grid are shown in Figure 13. Again, one sees that the 2nd-order central scheme has a higher error compared to the 2nd-order upwind scheme, even though both are 2nd-order accurate. The 3rd-order upwind U-MUSCL scheme with □=0.5 indeed reduces the solution error, but the error converges at a rate of 2.2 rather than 3.0.

Figure 14 displays the error convergence rate of the existing upwind convection scheme in FUN3D on the unstructured grid. It is clear the all schemes exhibit a convergence rate that is less than 3rd-order accurate.

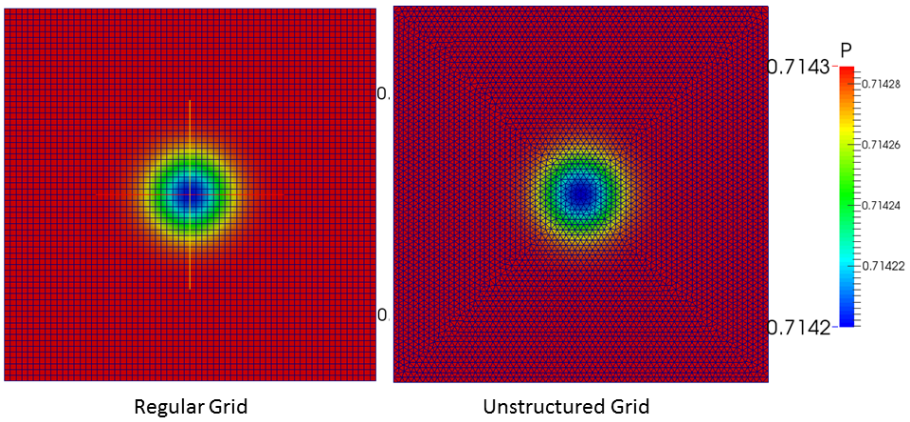

Figure 12. Simulation meshes for both regular and unstructured grids.

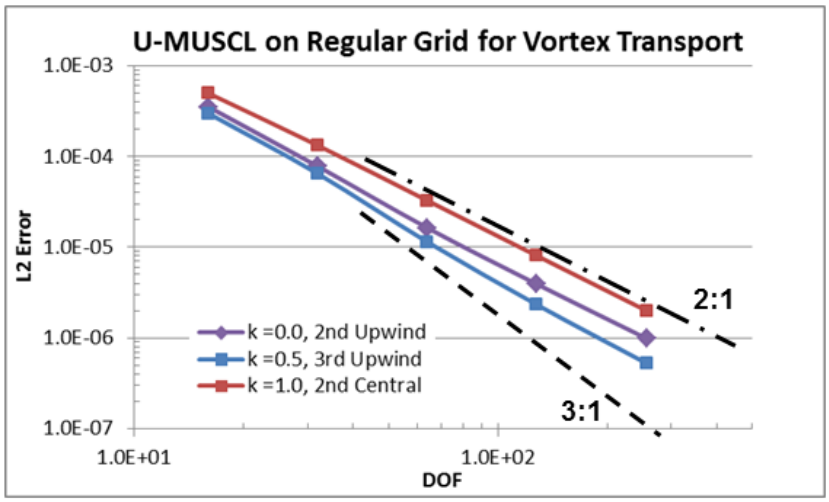

Figure 13. Error convergence of existing 2nd-order schemes in FUN3D for a 2D vortex transport problem on the regular grid.

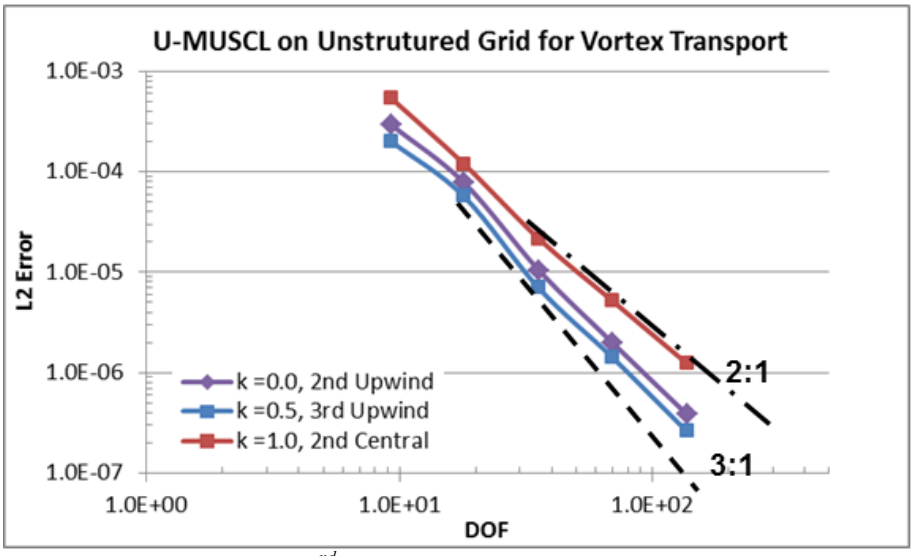

Figure 14. Error convergence of existing 2nd-order schemes in FUN3D for a 2D vortex transport problem on the unstructured grid.

IV. Derivation of High-Order Scheme for FUN3D

The present high-order scheme formulation under development for FUN3D builds on the existing FUN3D code structure. As shown in Equation (12), the functional form used in FUN3D is given by:

$$Q_i = Q_0 + \frac{\partial Q}{\partial x}(x_i - x_0) + \frac{\partial Q}{\partial y}(y_i - y_0), \tag{24}$$

and we propose to extend the above interpolation by adding high-order correction terms. For example, the functional form for a 3rd-order scheme is as follows:

$$Q^h(x,y) = Q(x_0,y_0) + \frac{\partial Q}{\partial x}(x-x_0) + \frac{\partial Q}{\partial y}(y-y_0) + \frac{1}{2}[\frac{\partial^2 Q}{\partial x^2}(x-x_0)^2 + 2\frac{\partial^2 Q}{\partial x \partial y}(x-x_0)(y-y_0) + \frac{\partial^2 Q}{\partial y^2}(y-y_0)^2]. \tag{25}$$

One notices that the first three terms on the right-hand side are the Q value of the existing scheme, but with the high-order correction:

$$\Delta Q^{h-2} = Q^h - Q^2 = \frac{1}{2}\left[\frac{\partial^2 Q}{\partial x^2}(x-x_0)^2 + 2\frac{\partial^2 Q}{\partial x^2}(x-x_0)(y-y_0) + \frac{\partial^2 Q}{\partial y^2}(y-y_0)^2\right]. \tag{26}$$

If we can determine this high-order correction, we can potentially improve the solution accuracy.

The high-order correction term to the variable Q requires knowledge of its second derivatives. If we can find the higher derivatives, we can achieve high-order accuracy. Our approach is to apply the Green theorem or least squares method to compute the higher derivatives. For a function h, we can write:

$$\frac{\partial h}{\partial x} = \frac{1}{\Omega}\oint_\Omega h dx; \quad \frac{\partial h}{\partial y} = \frac{1}{\Omega}\oint_\Omega h dy. \tag{27}$$

Since we already know the first derivative from the existing computation in the 2nd-order scheme, it is possible to determine the second derivatives directly. Using Green's theorem, as demonstrated in [21], we have:

$$\frac{\partial^2 Q}{\partial x^2} = \frac{1}{\Omega}\oint \frac{\partial Q}{\partial x} dx; \quad \frac{\partial^2 Q}{\partial x \partial y} = \frac{1}{\Omega}\oint \frac{\partial Q}{\partial x} dy; \quad \frac{\partial^2 Q}{\partial y^2} = \frac{1}{\Omega}\oint \frac{\partial Q}{\partial y} dy; \tag{28}$$

If the first derivatives are computed with the least squares approach, the same procedure as above can be used to compute the second derivatives based on the values of the first derivatives, i.e.:

$$\frac{\partial^2 Q}{\partial x^2} = \frac{\partial}{\partial x}\left(\frac{\partial Q}{\partial x}\right); \quad \frac{\partial^2 \mathbf{Q}}{\partial \mathbf{x} \partial \mathbf{y}} = \frac{\partial}{\partial y}\left(\frac{\partial Q}{\partial x}\right). \tag{29}$$

Figure 15 shows the cells involved in computing higher derivatives for a 2D vertex–centered triangular mesh.

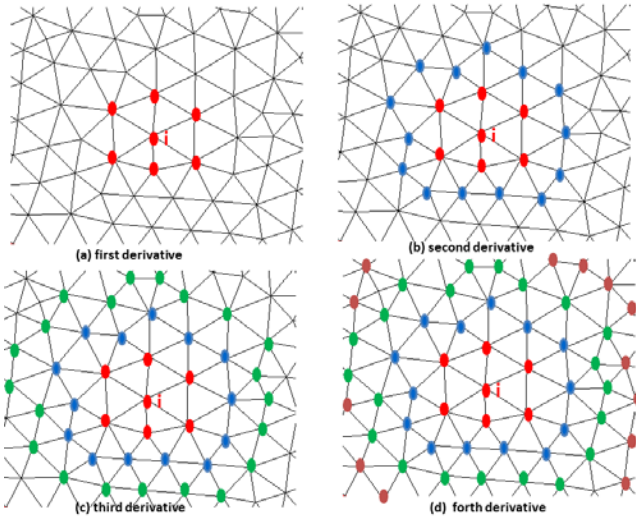

Figure 15. Neighbor cells required to compute derivatives using the current approach.

3rd-order U-MUSCL Scheme

Starting from the existing U-MUSCL scheme in FUN3D:

$$Q^{L}{}_{i+1/2} = Q_i + \frac{\kappa}{2}(Q_{i+1} - Q_i) + (1-\kappa)\vec{\nabla}Q_i \bullet \vec{r}_{fi} \,. \tag{30}$$

Our proposed 3rd-order U-MUSCL scheme is written in the similar fashion:

$$\begin{aligned} Q^{L}{}_{i+1/2} &= Q_i + \frac{\kappa}{2}(Q_{i+1} - Q_i) + (1-\kappa)\vec{\nabla}Q_i \bullet \vec{r}_{fi} + \frac{1}{2}\left[\frac{\kappa_3}{2}\left(\vec{\nabla}Q_{i+1} \bullet \vec{r}_{fi} - \vec{\nabla}Q_i \bullet \vec{r}_{fi}\right) + (1-\kappa_3)\vec{\nabla}\left(\vec{\nabla}Q_i \bullet \vec{r}_{fi}\right) \bullet \vec{r}_{fi}\right] \\ &= Q_i + \frac{\kappa}{2}(Q_{i+1} - Q_i) + (1-\kappa)\vec{\nabla}Q_i \bullet \vec{r}_{fi} \\ &\quad + \frac{1}{2}\left[\frac{\kappa_3 \Delta x_{fi}}{2}\left(\left(\frac{\partial Q}{\partial x}\right)_{i+1} - \left(\frac{\partial Q}{\partial x}\right)_i\right) + (1-\kappa_3)\Delta x_{fj}\vec{\nabla}\left(\frac{\partial Q}{\partial x}\right)_i \bullet \vec{r}_{fi}\right] \quad \text{Call \#1} \\ &\quad + \frac{1}{2}\left[\frac{\kappa_3 \Delta y_f i}{2}\left(\left(\frac{\partial Q}{\partial y}\right)_{i+1} - \left(\frac{\partial Q}{\partial y}\right)_i\right) + (1-\kappa_3)\Delta y_{fi}\vec{\nabla}\left(\frac{\partial Q}{\partial y}\right)_i \bullet \vec{r}_{fi}\right] \quad \text{Call \#2} \\ &\quad + \frac{1}{2}\left[\frac{\kappa_3 \Delta z_{fi}}{2}\left(\left(\frac{\partial Q}{\partial z}\right)_{i+1} - \left(\frac{\partial Q}{\partial z}\right)_i\right) + (1-\kappa_3)\Delta z_{fi}\vec{\nabla}\left(\frac{\partial Q}{\partial z}\right)_i \bullet \vec{r}_{fi}\right] \quad \text{Call \#3} \end{aligned} \tag{31}$$

As can be observed, one can use the same code structure that currently exists in FUN3D to compute the high-order corrections to the face values. By replacing the existing variable of Q by the first derivative in x ($\partial Q / \partial x$, for example), we can compute the second derivatives [21]:

$$\frac{\partial^2 Q}{\partial x^2}, \quad \frac{\partial^2 Q}{\partial x \partial y}, \quad \frac{\partial^2 Q}{\partial x \partial z}$$

Similarly, by calling the same routine using $\partial Q/\partial y$ and $\partial Q/\partial z$, we can find the contributions of:

$$\frac{\partial^2 Q}{\partial y \partial x}, \quad \frac{\partial^2 Q}{\partial y^2}, \quad \frac{\partial^2 Q}{\partial y \partial z} \quad \text{and} \quad \frac{\partial^2 Q}{\partial z \partial x}, \quad \frac{\partial^2 Q}{\partial z \partial y}, \quad \frac{\partial^2 Q}{\partial z^2}.$$

Order of Accuracy Analysis on 1D Uniform Grid

In this section, the above-proposed 3rd order U-MUSCL scheme is analyzed on a uniform 1D grid and optimal values of parameters for κ and κ_3 are determined. In 1D on a uniform grid, the least squares approximation to the gradient for interior nodes results in a gradient equal to the central differences gradient, so that:

$$\nabla Q_i \bullet \frac{\vec{r}}{2} = \frac{Q_{i+1} - Q_{i-1}}{4}; \quad \nabla Q_{i+1} \bullet \frac{\vec{r}}{2} = \frac{Q_{i+2} - Q_i}{4}. \tag{32}$$

With this expression, we can have:

$$
\begin{aligned}
Q^{L}{}_{i+1/2} &= Q_i + \frac{\kappa}{2}(Q_{i+1}-Q_i) + (1-\kappa)\bar{\nabla}Q_i \bullet \vec{r}_{fi} + \frac{1}{2}[\frac{\kappa_3}{2}(\bar{\nabla}Q_{i+1}-\bar{\nabla}Q_i)\bullet\vec{r}_{fi} + (1-\kappa_3)\bar{\nabla}(\nabla Q_i \bullet \vec{r}_{fi})\bullet\vec{r}_{fi}] \\
&= \mathrm{Q_i} + \frac{\kappa}{2}(Q_{i+1}-Q_i) + \frac{(1-\kappa)}{4}(Q_{i+1}-Q_{i-1}) + \frac{1}{2}[\frac{\kappa_3}{8}(Q_{i+2}-Q_{i+1}-Q_i+Q_{i-1}) + \frac{(1-\kappa_3)}{16}(Q_{i+2}-2Q_i+Q_{i-2})] \\
&= \frac{1+\kappa_3}{32}Q_{i+2} + \frac{4(1+\kappa)-\kappa_3}{16}Q_{i+1} + \frac{15-8\kappa}{16}Q_i + \frac{-4(1-\kappa)+\kappa_3}{16}Q_{i-1} + \frac{(1-\kappa_3)}{32}Q_{i-2} \\
&= \frac{1+\kappa_3}{32}\left(Q_{i+1/2} + Q'_{i+1/2}\frac{3\Delta x}{2} + Q''_{i+1/2}\frac{9\Delta x^2}{8} + Q'''_{i+1/2}\frac{27\Delta x^3}{48} + Q^{(4)}{}_{i+1/2}\frac{81\Delta x^4}{384} + O(\Delta x^5)\right) \\
&\quad + \frac{4(1+\kappa)-\kappa_3}{16}\left(Q_{i+1/2} + Q'_{i+1/2}\frac{\Delta x}{2} + Q''_{i+1/2}\frac{\Delta x^2}{8} + Q'''_{i+1/2}\frac{\Delta x^3}{48} + Q^{(4)}{}_{i+1/2}\frac{\Delta x^4}{384} + O(\Delta x^5)\right) \\
&\quad + \frac{15-8\kappa}{16}\left(Q_{i+1/2} - Q'_{i+1/2}\frac{\Delta x}{2} + Q''_{i+1/2}\frac{\Delta x^2}{8} - Q'''_{i+1/2}\frac{\Delta x^3}{48} + Q^{(4)}{}_{i+1/2}\frac{\Delta x^4}{384} + O(\Delta x^5)\right) \\
&\quad + \frac{-4(1-\kappa)+\kappa_3}{16}\left(Q_{i+1/2} - Q'_{i+1/2}\frac{3\Delta x}{2} + Q''_{i+1/2}\frac{9\Delta x^2}{8} - Q'''_{i+1/2}\frac{27\Delta x^3}{48} + Q^{(4)}{}_{i+1/2}\frac{81\Delta x^4}{384} + O(\Delta x^5)\right) \\
&\quad + \frac{1-\kappa_3}{32}\left(\mathrm{Q}_{i+1/2} - \mathrm{Q}'_{i+1/2}\frac{5\Delta x}{2} + \mathrm{Q}''_{i+1/2}\frac{25\Delta x^2}{8} - \mathrm{Q}'''_{i+1/2}\frac{125\Delta x^3}{48} + \mathrm{Q}^{(4)}{}_{i+1/2}\frac{625\Delta x^4}{384} + \mathrm{O}(\Delta x^5)\right) \\
&= \mathrm{Q}_{i+1/2} + \frac{\kappa}{4}Q''_{i+1/2}\Delta x^2 + \frac{1-2\kappa+\kappa_3}{16}Q'''_{i+1/2}\Delta x^3 + \frac{3+20\kappa-12\kappa_3}{384}Q^{(4)}{}_{i+1/2}\Delta x^4 + O(\Delta x^5)
\end{aligned}
\tag{33}
$$

This formula represents a two-parameter family for the approximation of the face value of a variable. One can observe that:

- The scheme is at least 2nd-order accurate;
- When κ=0, the interpolation is 3rd-order accurate;
- When κ=0, and κ_3=-1, the interpolation is 4th-order accurate, with no dissipation; and
- By setting κ=0 and κ_3=-1+δ, where δ is a small quantity, one can introduce low damping and simultaneously maintain the high-order accuracy.

Approximation of the Derivative at the Node

With the face value given as in Equation (33), one can approximate the derivatives at the node as:

$$
\begin{aligned}
&\int_{x-1/2}^{x+1/2}\frac{\partial Q}{\partial x}dx \approx Q^{L}{}_{i+1/2} - Q^{L}{}_{i-1/2} \\
&= \frac{1+\kappa_3}{32}Q_{i+2} + \frac{7+8\kappa-3\kappa_3}{32}Q_{i+1} + \frac{11-12\kappa+\kappa_3}{16}Q_i + \frac{-19+12\kappa+\kappa_3}{16}Q_{i-1} + \frac{9-8\kappa-3\kappa_3}{32}Q_{i-2} + \frac{-1+\kappa_3}{32}Q_{i-3} \\
&= Q'_i\,\Delta x + \frac{1+6\kappa}{24}Q'''_i\,\Delta x^3 + \frac{1-2\kappa+\kappa_3}{16}Q_i{}^{(4)}\Delta x^4 + O(\Delta x^5)
\end{aligned}
\tag{34}
$$

One can see that:

- The formula is at least 2nd-order accurate;
- When κ=-1/6, approximating the derivative at the cell center is the third-order accurate;
- When κ=-1/6, and κ_3=-4/3, the interpolation is 4th-order accurate, with no dissipation;
- By setting κ=-1/6 and κ_3=-4/3+δ, where δ is a small quantity, one can introduce low damping and simultaneously maintain the high-order accuracy.

Fourier Analysis of 3rd-Order U-MUSCL Scheme

The Fourier analysis technique is used in this section to quantify the dissipation and dispersion errors of the proposed 3rd-order U-MUSCL scheme. Fourier analysis provides effective insight into the dissipation and dispersion properties of the current high-order scheme, and may be used to further guide the optimization of the scheme.

The Fourier transformation of Equation (34) is:

$$i\omega\Delta x = \left[\frac{1+k_3}{32}\exp(2i\omega\Delta x) + \frac{7+8k-3k_3}{32}\exp(i\omega\Delta x) + \frac{11-12k+k_3}{16} + \frac{-19+12k+k_3}{16}\exp(-i\omega\Delta x) + \frac{9-8k-3k_3}{32}\exp(-2i\omega\Delta x) + \frac{-1+k_3}{32}\exp(-3i\omega\Delta x)\right] \tag{35}$$

and from the above expression, the modified wavenumber can be derived as:

$$\overline{\omega}\Delta x = \frac{-8+8k+4k_3}{32}\sin(2\omega\Delta x) + \frac{45-16k-5k_3}{32}\sin(\omega\Delta x) + \frac{1-k_3}{32}\sin(3\omega\Delta x) \tag{36}$$

Figure 16 shows a comparison of results for the present 3rd-order U-MUSCL scheme to those of other well-known central-type schemes and the existing U-MUSCL scheme in FUN3D. One can see that the standard unstructured 2nd-order upwind scheme, which corresponds to the U-MUSCL scheme in FUN3D at κ=0, has reduced dispersion over the standard 2nd- and 4th-order central scheme. But as will be shown later, the results contain more numerical damping. The proposed 3rd-order U-MUSCL scheme has the lowest dispersion error in comparison to all other schemes, including the standard 6th-order central scheme. This dispersion property enables the scheme to resolve high-frequency waves.

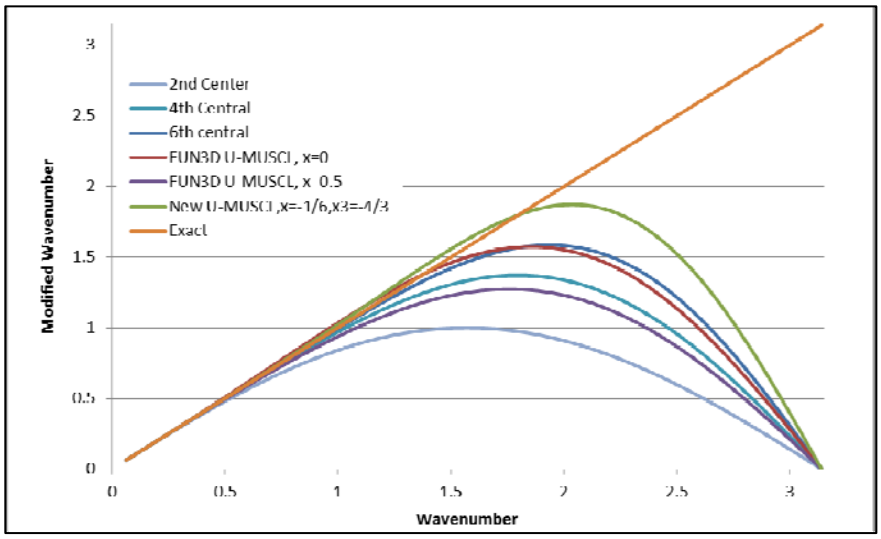

Figure 16. Modified wavenumber vs. true wavenumber for various schemes.

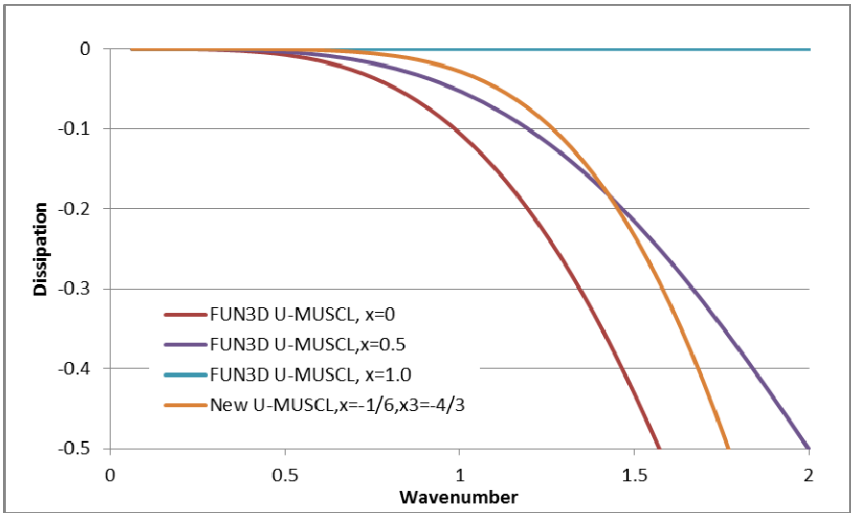

Figure 17. Dissipation of various schemes as a function of wavenumber.

Figure 17 shows the dissipation properties for various different schemes. The existing schemes in FUN3D at κ=1.0 are 2nd-order central-type schemes and have no damping. As seen from Figure 16, the 2nd-order central scheme has the largest dispersion error, while the standard 2nd-order upwind scheme at κ=0.0 the scheme contains very high dissipation even though it has low dispersion. For the present 3rd-order U-MUSCL scheme, the dissipation is rather low in comparison to all others, and the new scheme performs well even for the wavenumber up to 0.7.

V. Results for High-Order U-MUSCL Schemes

Solution of High-Order Scheme for 1D Acoustic Problem

The above 3rd-order U-MUSCL scheme module has been implemented in FUN3D, and initial assessments are made using a simple 1D acoustic problem. Shown in Figure 18 is a comparison of results for the new scheme against those for the existing 2nd-order schemes in FUN3D on a regular grid. As derived above, on the regular grid with uniform spacing, the present 3rd-order U-MUSCL scheme is 4th-order accurate, and the error drops very rapidly with grid refinement. The savings is significant as one can observe that by using this 3rd-order scheme with 32 grid points, one can get as accurate a result as that obtained from using 128 grid points with the existing scheme. Previous studies have found that for sufficient grid resolution using 2nd-order schemes, 16 points per wavelength are necessary. As illustrated in Figure 18, one needs only 8 points per wavelength when using the 3th-order U-MUSCL scheme to achieve the same L_2 error.

Results of the present high-order scheme for the 1D acoustic problem on *triangular grids* are shown in Figure 19. It is apparent that the new scheme exhibits the lowest error and has a superior convergence rate than the existing schemes. On the triangular grid, the grid spacing is no longer uniform and some lower order errors persist rather than being canceled out. As a result, the error converges at a 3rd-order rate. Even so, the error is much lower than the existing 2nd-order schemes in FUN3D. One can see that with 16 points the present 3rd-order U-MUSCL scheme can provide the same resolution as the existing 2nd-order scheme with 32 points.

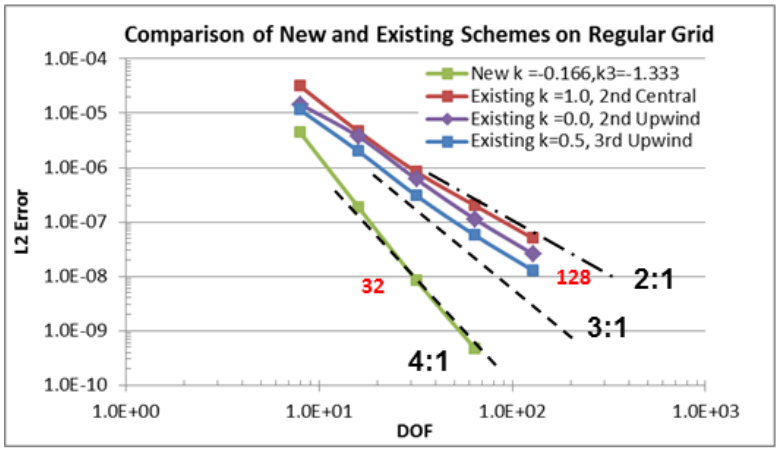

Figure 18. Comparison of new and existing schemes in FUN3D on a regular grid for the 1D acoustic problem.

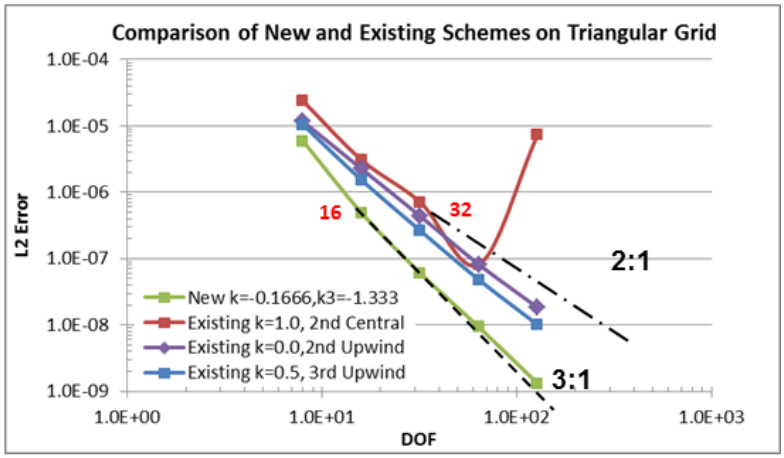

Figure 19. Comparison of new and existing schemes in FUN3D on the triangular grid for the 1D acoustic problem.

Solution of High-Order Scheme for 2D Vortex Transport Problem

Figure 20 shows the application of the new scheme to a 2D vortex transport problem on regular structured grids. Again we can see improved solution accuracy over the existing schemes. For example, results for the new scheme on a 64x64 grid are as accurate as those for the existing 2nd-order scheme on a 256x256 grid.

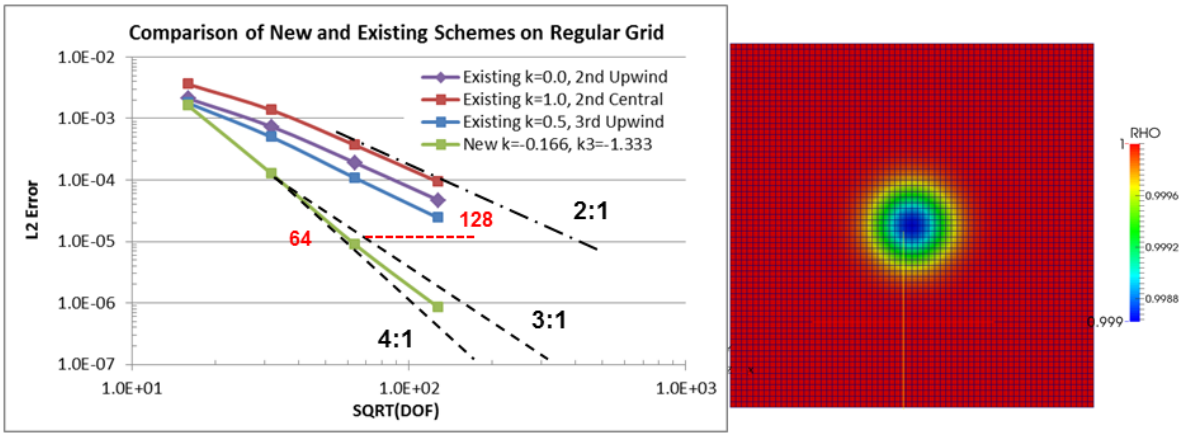

Figure 20. Comparison of new and existing schemes in FUN3D on a regular grid for 2D vortex transport problem.

The results on a triangular grid are given in Figure 21, and it is observed that the convergence rate is 3rd-order. Figure 22 shows the velocity profile for several different cases where the vortex is transported for 10 cycles through the domain on the unstructured grid, and the improvements provided by the high-order scheme are profound. As the fluid viscosity is zero, the vortex should maintain its strength and be passively convected with the uniform flow. However, due to the dissipation and dispersion errors of the 2nd-order scheme, the strength of the vortex has been weakened as evident from the magnitude of the velocity profile obtained when using a grid comprised of 1/32x1/32-sized cells. On the other hand, the 3rd-order scheme can maintain the vortex strength very well, and it provides similar accuracy to the 2nd-order upwind scheme when using 1/64x1/64-sized cells. The computed velocity profiles along the center line are given in Figure 23.

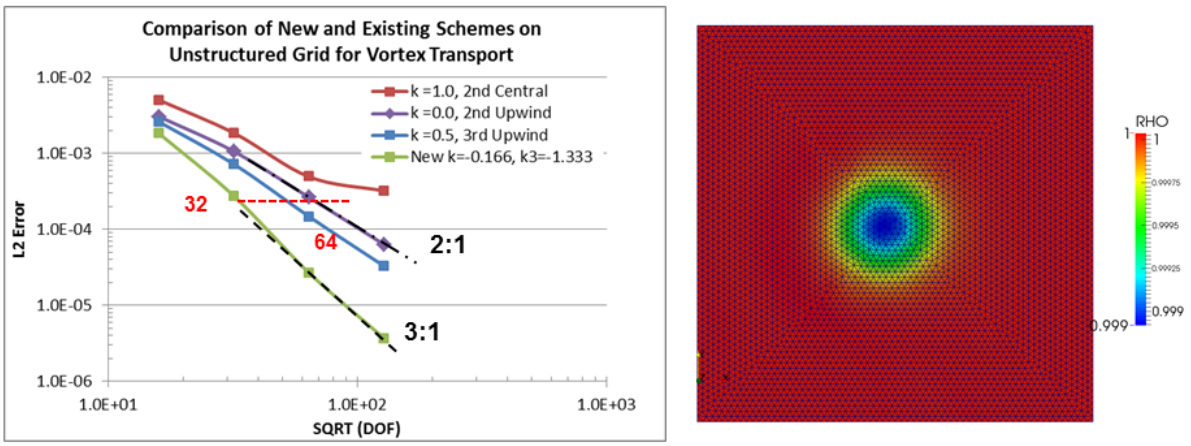

Figure 21. Comparison of new and existing schemes in FUN3D on unstructured grid for 2D vortex transport problem.

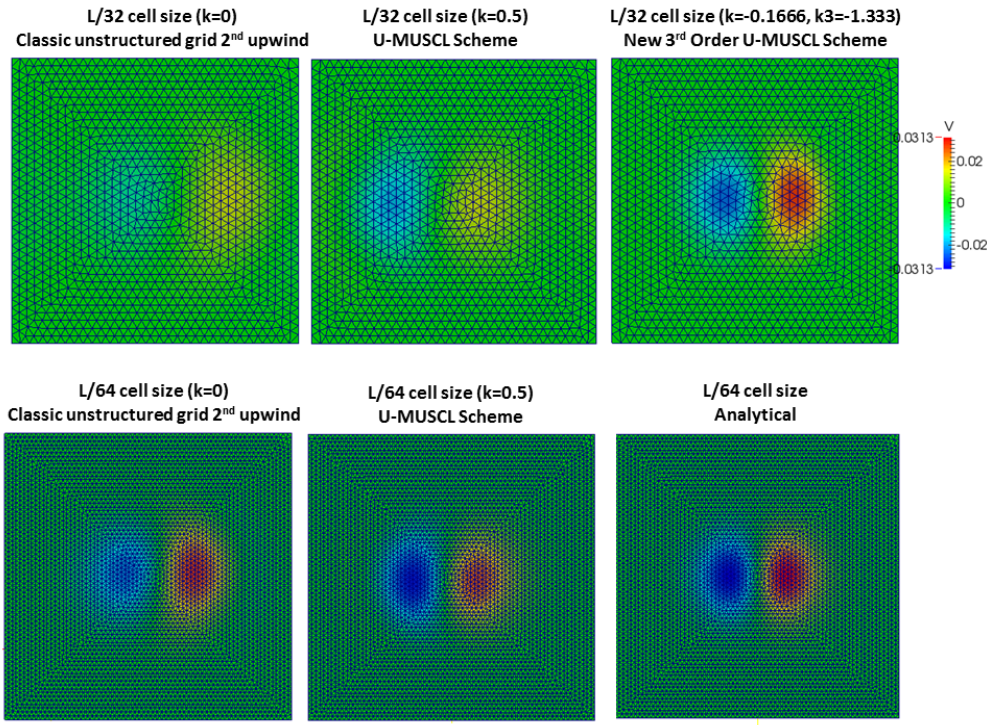

Figure 22. Comparison of vertical velocity component distribution computed by the new high-order scheme and the existing schemes on unstructured grid after 10 cycles of convection.

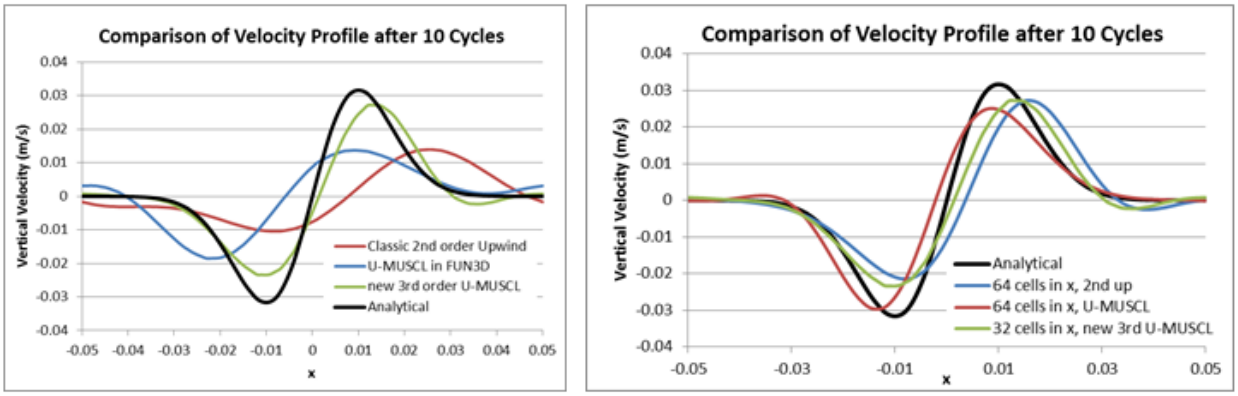

Figure 23. Comparison of vertical velocity component profile computed by the new high-order scheme and the existing schemes on unstructured grid after 10 cycles of convection.

Solution of Two Cylinder Acoustic Wave Diffraction on Unstructured Grids

As a verification of the new scheme in FUN3D for propagation and scattering of acoustic waves around complex geometries, the two cylinder acoustic diffraction problem from the Fourth Computational Aeroacoustics (CAA) Workshop on Benchmark Problems is considered [29]. The transient acoustic source term used, in this case, is expressed in the following form

$$S = \exp\left[-\ln 2 * \left\{\frac{x_S^2 + y_S^2}{b^2}\right\}\right] \sin(\omega t), \tag{37}$$

where ω=8π, b=02, t is time, and the spatial coordinates, x_S and y_S, are expressed relative to the center of the acoustic source, respectively. In the present study, the above source term is added to the energy equation of the nonlinear Euler equations. According to the non-dimensional problem setup, the acoustic source is physically positioned 4 units to the right of a cylinder of diameter=1.0 and 4 units to the left of a cylinder of diameter=0.5. This arrangement is shown in Figure 24 for clarity.

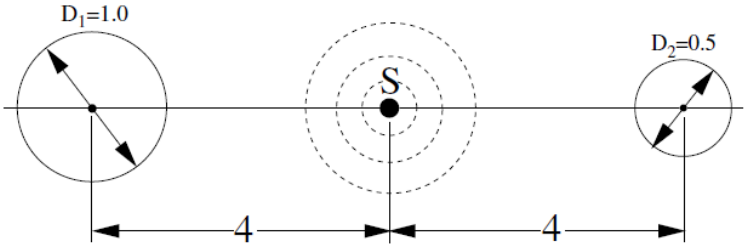

Figure 24. Schematic illustrating location of time-dependent acoustic source and relative cylinder sizes for two cylinder acoustic scattering problem.

Outer domain extents are chosen to be 50 diameters (with respect to the largest cylinder) from the acoustic source to ensure that numerical boundary conditions applied at the outer boundary are sufficiently removed so as to avoid nonphysical waves from polluting the field. Two different grids are generated for this case. These grids are comprised of triangular cells that have been extruded by one cell in the third dimension to produce a 3D triangular prism grid that is one cell thick. The coarsest grid has a spacing of h=0.04 and is comprised of 105K cells, and the finer grid has a spacing of h=0.02 and is comprised of 423K cells. In the discussion to follow, the coarsest grid is referred to as *grid01* and the finer grid is referred to as *grid02*. Two different views of *grid01* are shown in Figure 25.

The solution is initialized to be an essentially zero velocity condition (M_∞=1e-8) and with T_∞=300K. All simulations are carried out using a fixed time step size of Δt=0.002 seconds for 20,000-time steps using 6 subiterations. Statistics are computed for the last 2,000 steps of the simulation for use in comparing against the analytical solution [29]. Three different simulations are carried out to test the existing 2nd-order U-MUSCL scheme in FUN3D, as well as compare with the new U-MUSCL scheme with 3rd-order interpolation. First, 2nd-order simulations are carried out using the default U-MUSCL scheme on both *grid01* (105K cells) and *grid02* (423K cells). After that, simulations are carried out using the new U-MUSCL scheme with 3rd-order interpolation on *grid01*. The default U-MUSCL κ parameter and standard 2nd-order time integration is used for the 2nd-order simulations, whereas κ=-1/6 and κ_3=-4/3 and 3rd-order-time integration is used for the simulations employing the 3rd-order interpolation.

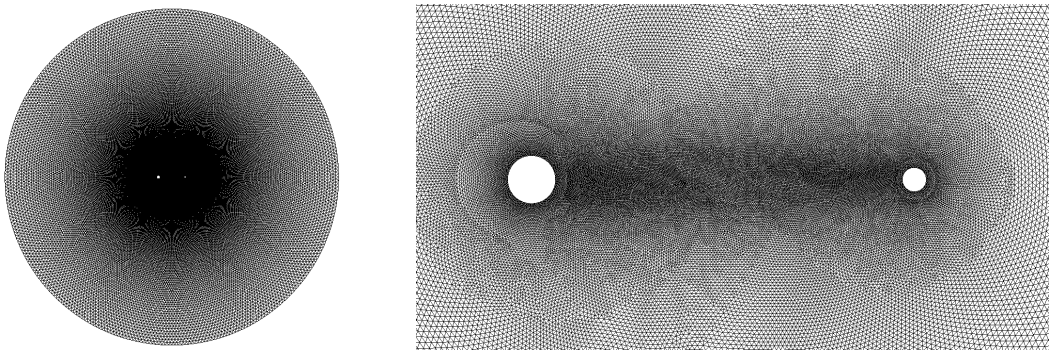

Figure 25. Views of grid01 (coarsest grid) for two cylinder acoustic scattering simulations.

The final pressure field computed using the default 2nd-order FUN3D U-MUSCL scheme on *grid01* (top left) and *grid02* (top right) is shown in Figure 26, along with that computed using the new U-MUSCL scheme with 3rd-order interpolation (bottom). It is apparent that the acoustic source is rapidly dissipated in the results on *grid01* when using the default 2nd-order U-MUSCL scheme such that a scattering field between the cylinders is never quite realized, whereas the 2nd-order results on *grid02* exhibit substantially less dissipation, and a scattering field is observed between the cylinders. As evidenced in the bottom of Figure 26, the addition of the 3rd-order interpolation U-MUSCL approach has markedly improved the resolution of the 2nd-order simulation.

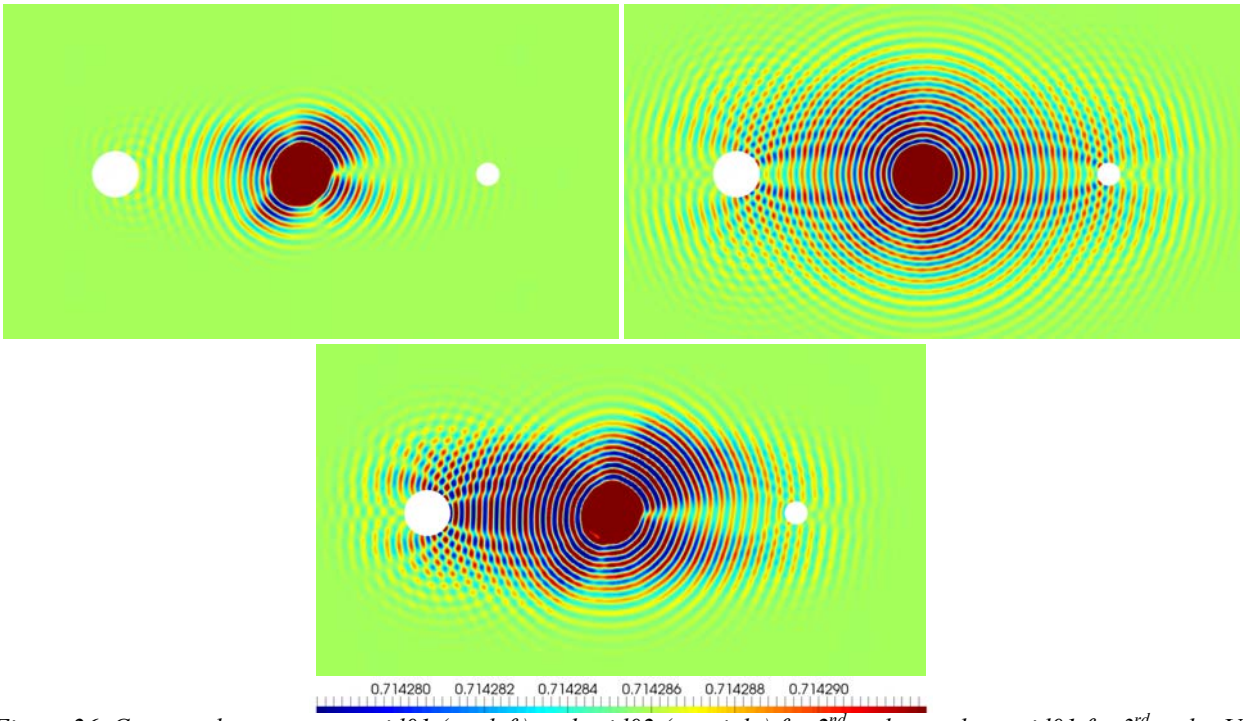

Figure 26. Computed pressure on grid01 (top left) and grid02 (top right) for 2nd order, and on grid01 for 3rd order U-MUSCL interpolation, for simulation of two cylinder acoustic scattering.

The analytical solution for the RMS pressure along the centerline is presented in Figure 27 (left) along with the computed default 2nd-order U-MUSCL scheme results on both *grid01* and *grid02* (right). The results are all presented at three different magnification levels, with magnification increasing from top to bottom in the figure. It is apparent that *grid01* provides insufficient resolution to permit accurate simulation of acoustic propagation when using the default 2nd-order U-MUSCL scheme due to the large errors observed in the RMS pressure away from the acoustic source. The results on *grid02* are considerably more accurate and very closely match with the analytical solution between the cylinders. While *grid02* provides considerably more resolution than *grid01* in between the cylinders, both grids are largely unable to resolve the RMS pressure on the downstream side of the cylinders. This indicates that a grid even finer than *grid02* would be required to achieve grid independence when using the default 2nd-order U-MUSCL scheme.

The computed centerline RMS pressure for the default 2nd-order and 3rd-order interpolation U-MUSCL schemes on *grid01* are presented in Figure 28 (left), along with results for the default 2nd-order scheme on *grid02* and the 3rd-order interpolation U-MUSCL scheme on *grid01* (right). While the results for the 3rd-order interpolation U-MUSCL scheme on *grid01* provide slightly less resolution than the default 2nd-order U-MUSCL scheme on *grid02*, the benefits of the 3rd-order interpolation are still quite profound. The 3rd-order interpolation U-MUSCL solution on *grid01* with more than 75% fewer computational cells than *grid02* exhibits a tremendous increase in accuracy over the standard 2nd-order U-MUSCL scheme and is actually approaching the accuracy of the 2nd-order scheme on *grid02*. All things considered, the 3rd-order interpolation U-MUSCL scheme is vastly superior to the standard 2nd-order scheme on a given grid.

Up to this point, the results presented for the 3rd-order interpolation U-MUSCL approach have made use of existing midpoint rules for computation of all flux integrals. Since the polynomial reconstruction of the solution for the 3rd-order approach includes higher-order gradients and is thus non-linear, the face-averaged solution can no longer be taken to be the solution value at the face center. To ensure that accuracy is not lost during the flux integration for the 3rd-order scheme, an improved flux integration procedure is introduced that makes use of high-order Gaussian quadrature rules rather than the midpoint rule. In the FUN3D vertex-centered finite-volume approach, the flux integration for each edge involves a collection of triangular faces that is constructed by connecting the edge center with each of the neighboring face and cell centers forming the so-called dual-mesh. For 2nd-order schemes, the area and normal of the collection of triangular faces is computed as a weighted average across the set, and for the purposes of computing the flux integral, each edge center is treated as an effective face with that area and normal vector. For the 3rd-order U-MUSCL approach, the collection of triangular faces associated with

each edge is retained, and either 1-point or 3-point Gauss quadrature rules are invoked to carry out the flux integration over the triangular faces with high-order accuracy.

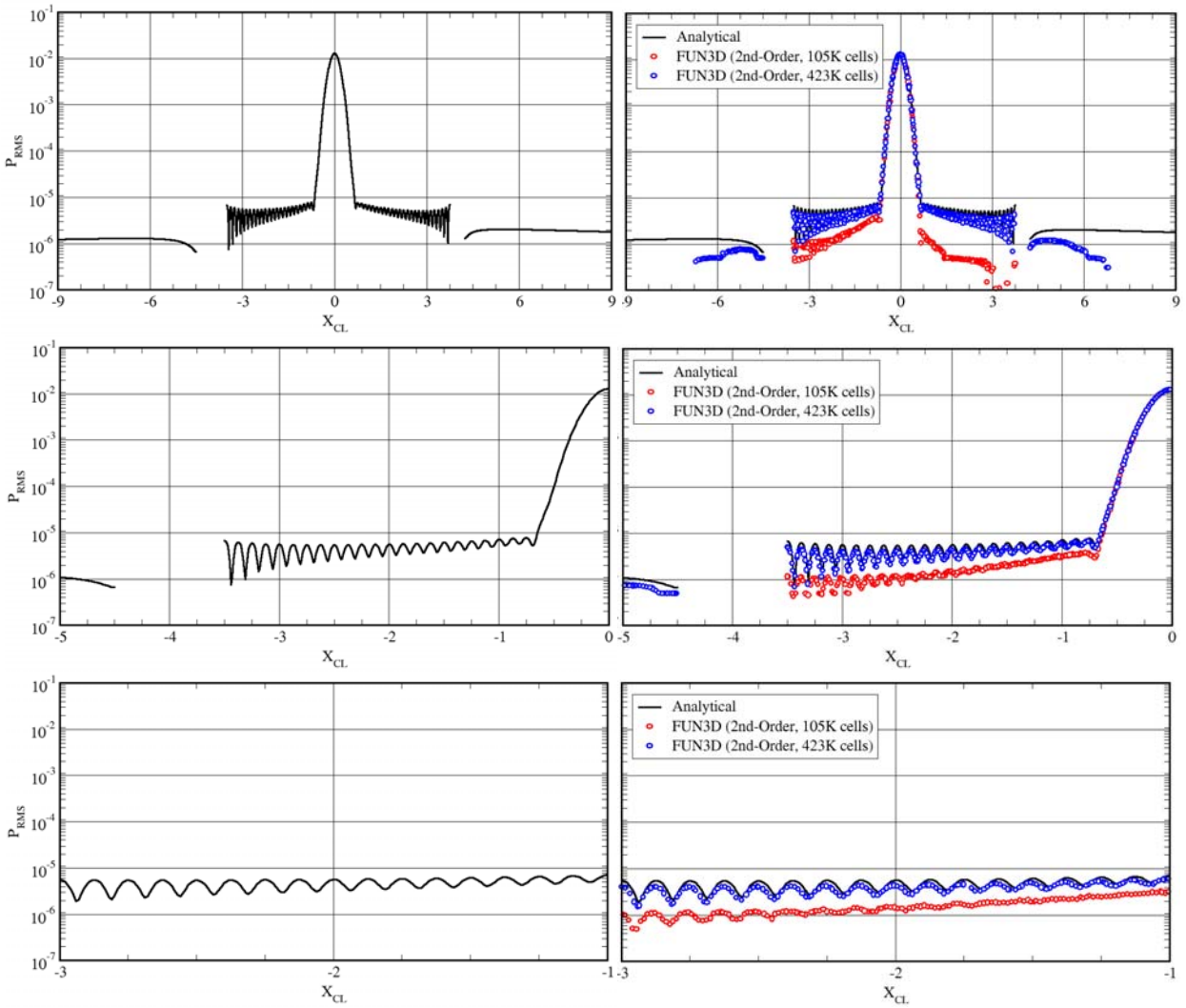

Figure 27. Views of increasing magnification (top to bottom) of centerline RMS Pressure for two-cylinder acoustic scattering: (left) analytical solution; and (right) comparison of analytical solution (black) and default 2nd-order U-MUSCL approach on grid01 (red) and grid02 (blue).

Making use of the Gauss quadrature flux integration procedure, the two cylinder acoustic scattering case is revisited. Figure 29 shows the computed pressure field on *Grid01* using the 2nd-order scheme, 3rd-order interpolation U-MUSCL scheme, 3rd-order interpolation U-MUSCL scheme with 3-point Gauss quadrature flux integration, and the 2nd-order scheme on *Grid02*. A slightly improved resolution of the pressure signal is observed when using the Gauss quadrature integration, which is most readily discernible near the right cylinder.

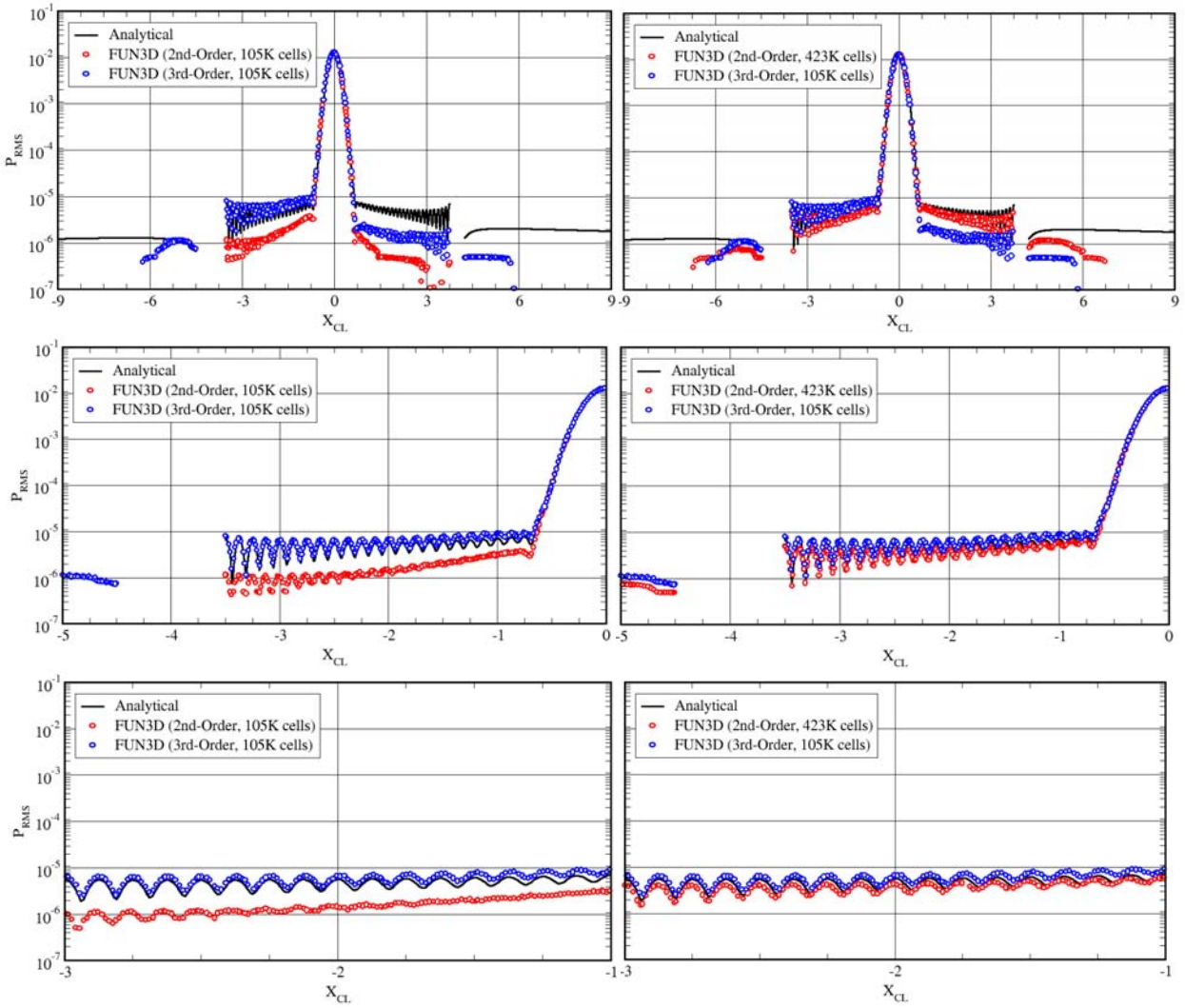

Figure 28. Views of increasing magnification (top to bottom) of centerline RMS Pressure for two-cylinder acoustic scattering: (left) comparison of analytical solution (black), default 2nd-order U-MUSCL (red) and 3rd-order interpolation U-MUSCL approaches (blue) on grid01; and (right) comparison of analytical solution (black), default 2nd-order U-MUSCL approach on grid02 (red), and 3rd-order interpolation U-MUSCL approach on grid01 (blue).

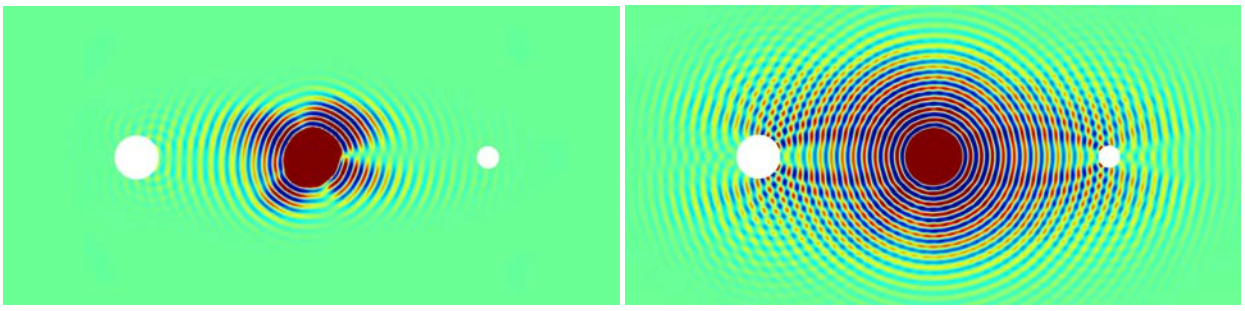

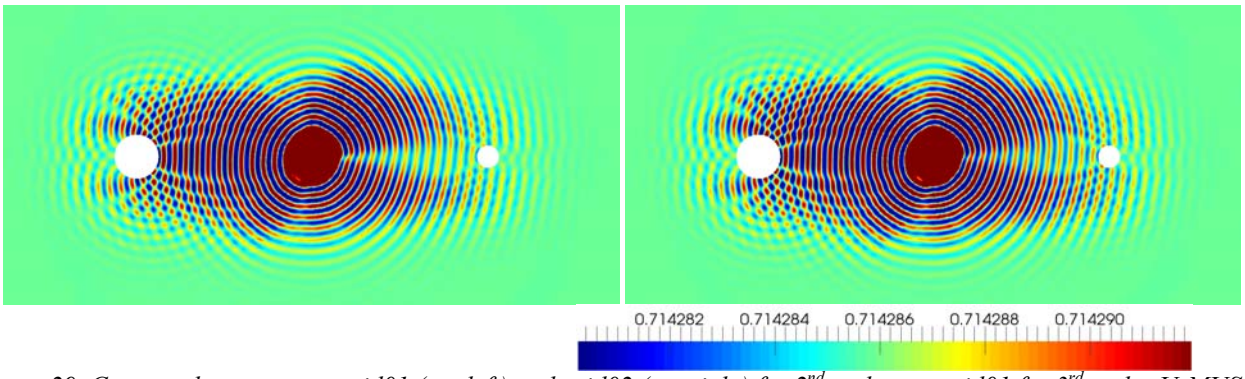

Figure 29. Computed pressure on grid01 (top left) and grid02 (top right) for 2nd-order, on grid01 for 3rd-order U-MUSCL interpolation (bottom left), and on grid01 for 3rd-order U-MUSCL interpolation with Gauss quadrature flux integration (bottom right), for simulation of two cylinder acoustic scattering.

Figure 30 shows the computed centerline RMS pressure for the various scheme with results using 1-point quadrature on the left and those using 3-point quadrature on the right. Since there is little to no observable difference between results computed using 1-point (i.e. midpoint) and 3-point Gauss quadrature rules, the additional resolution present simply from integrating on the triangles themselves has dramatically improved the accuracy of the 3rd-order scheme for predicting the centerline RMS pressure. Dramatically improved predictions compared to the analytical solution are visible downstream of both cylinders as well as between the acoustic pulse and right cylinder where the diffraction pattern is more difficult to predict.

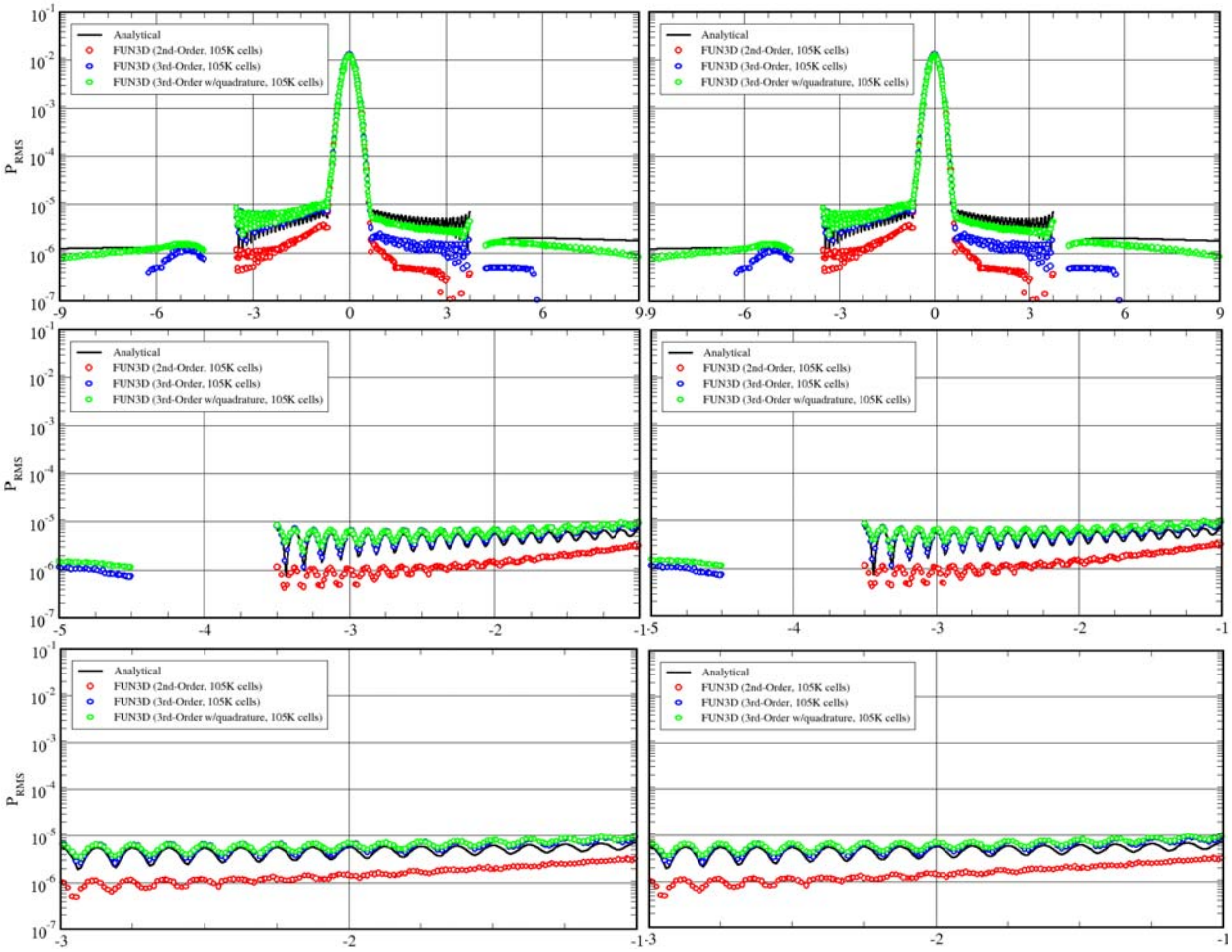

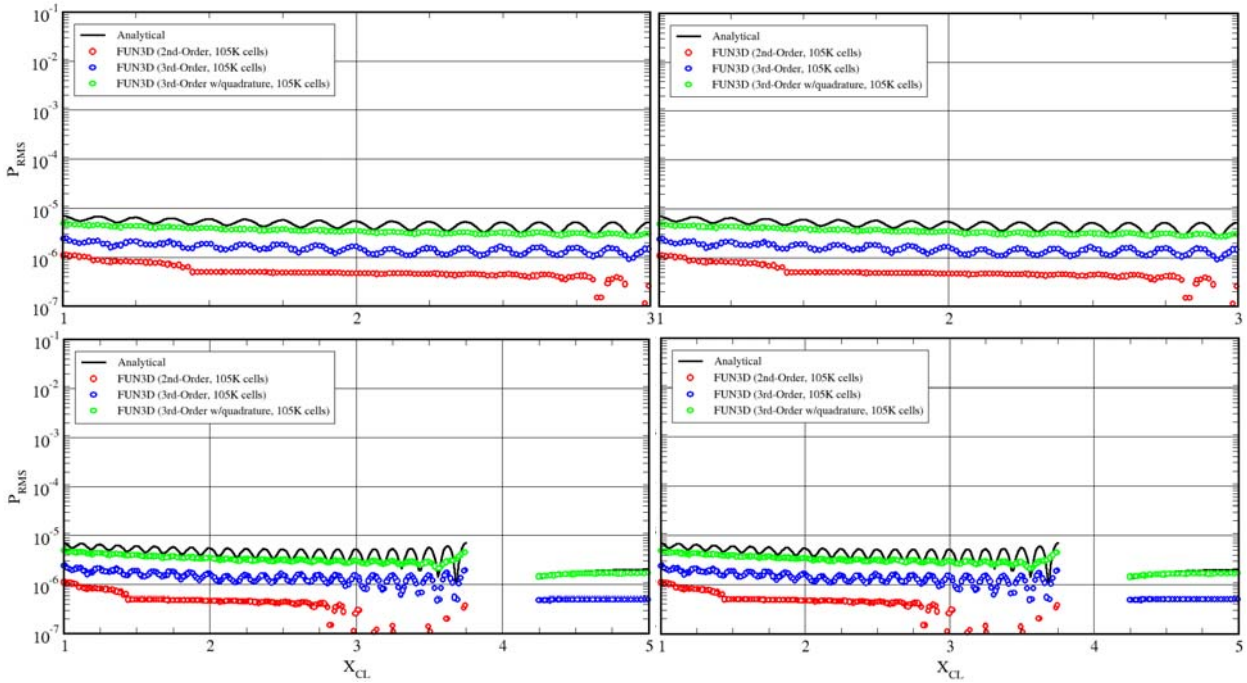

Figure 30. Various views of centerline RMS Pressure for two-cylinder acoustic scattering using Gauss quadrature for flux integration: (left) 1 point quadrature; and (right) 3 point quadrature.

3D Taylor-Green Vortex Transition to Turbulence

The spatial and temporal evolution of a Taylor-Green vortex flow in a three-dimensional periodic domain is a good model to investigate the accuracy of high-order schemes. The problem involves the nonlinear transfer of kinetic energy among eddies with a range of spatial scales. When the flow has a finite Reynolds number, the kinetic energy generated by velocity shear is dissipated by the smallest scales, which provides a simple model for the development of a turbulent flow and the cascade of energy from larger to smaller scales. The Taylor-Green vortex is a fundamental case that has been traditionally used as a prototype for vortex stretching and consequent production of small scale eddies, to investigate the basic dynamics of transition to turbulence based on DNS [30].

Computational Model

The Taylor-Green vortex configuration considered here involves triple-periodic boundary conditions enforced on a cubic domain with box side length of 2π. The initial condition is smooth and consists of a first-degree trigonometric polynomial in all three directions as:

$$u = u_0 \cos(x)\sin(y)\sin(z)e^{-2\nu t}; v = -u_0 \sin(x)\cos(y)\sin(z)e^{-2\nu t}$$
$$w = 0; p = -\frac{\rho {u_0}^2}{4}(\cos 2x + \cos(2y))e^{-4\nu t} \quad (38)$$

Here the u_0 is chosen as M=0.1, and the initial condition in terms of vorticity isosurfaces is illustrated in Figure 31. Enclosed within each surface are regions of positive or negative vorticity.

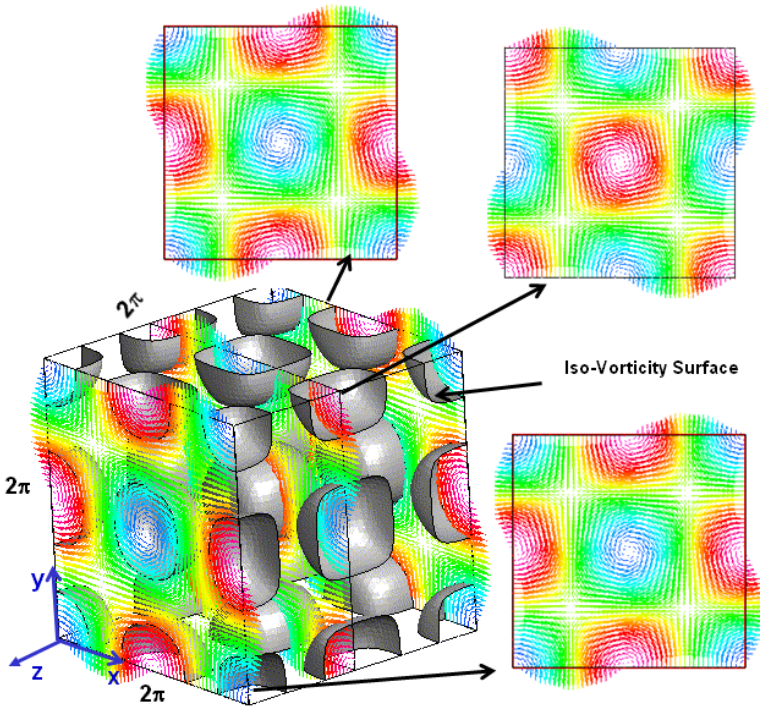

Figure 31. Initial vortical flow field for Taylor-Green Vortex.

For a simulation over a long time duration, a numerical scheme should accurately capture the behavior of the flow field as long as possible. The 2nd-order temporal scheme and 2nd- and 3rd-order spatial schemes are used to simulate the dynamic process of the vortex transition. The Reynolds number is 1,600 for this problem, and the simulations are carried out for the space of 2π in the x direction but π rather than standard 2π in the other two directions. Three different grids comprised of triangular prism cells are used, with resolution of 1.2M, 4.5M, and 9.0 M, as shown in Figure 32. Periodic boundary conditions are imposed in the x-direction and symmetry conditions are used on the other boundaries.

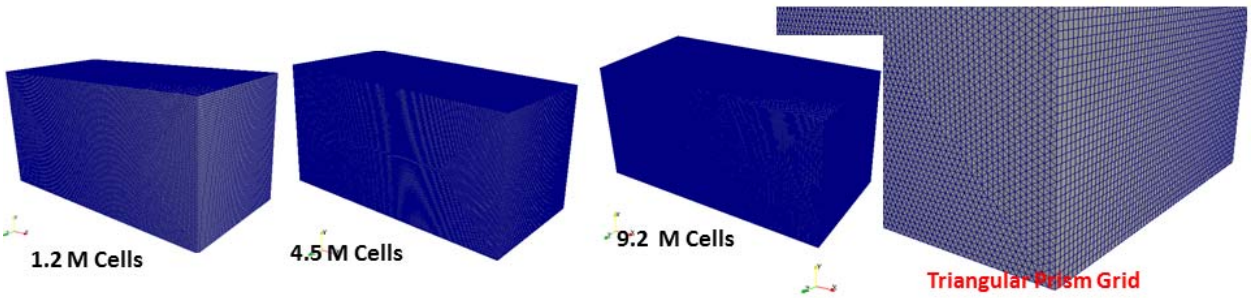

Figure 32. Three triangular prism grids with different resolution.

Figure 33 shows Q isosurfaces representing transition of vortical flow to turbulence at different time instances. To appreciate the increase of solution accuracy due to the high-order scheme, Figure 34 gives the Q isosurface at dimensionless time of 20 obtained when using the existing 2nd-order scheme and the low dissipation 3rd-order scheme. It is apparent that the 2nd-order scheme contains significant numerical dissipation, and the size of the resolved vortical flow structure is rather large when using 1.2M cells. With the use of 5.2M cells, the resolution increases and the size becomes even smaller on the 9.2M cell grid. On the other hand, when using 1.2M grid cells with the low dissipation 3rd-order scheme, the resolution is as good as that obtained on the 9.2M cell grid when using the 2nd-order scheme. In terms of the required grid cell count to achieve a particular accuracy level, a factor of 8 increase is provided by the 3rd-order scheme.

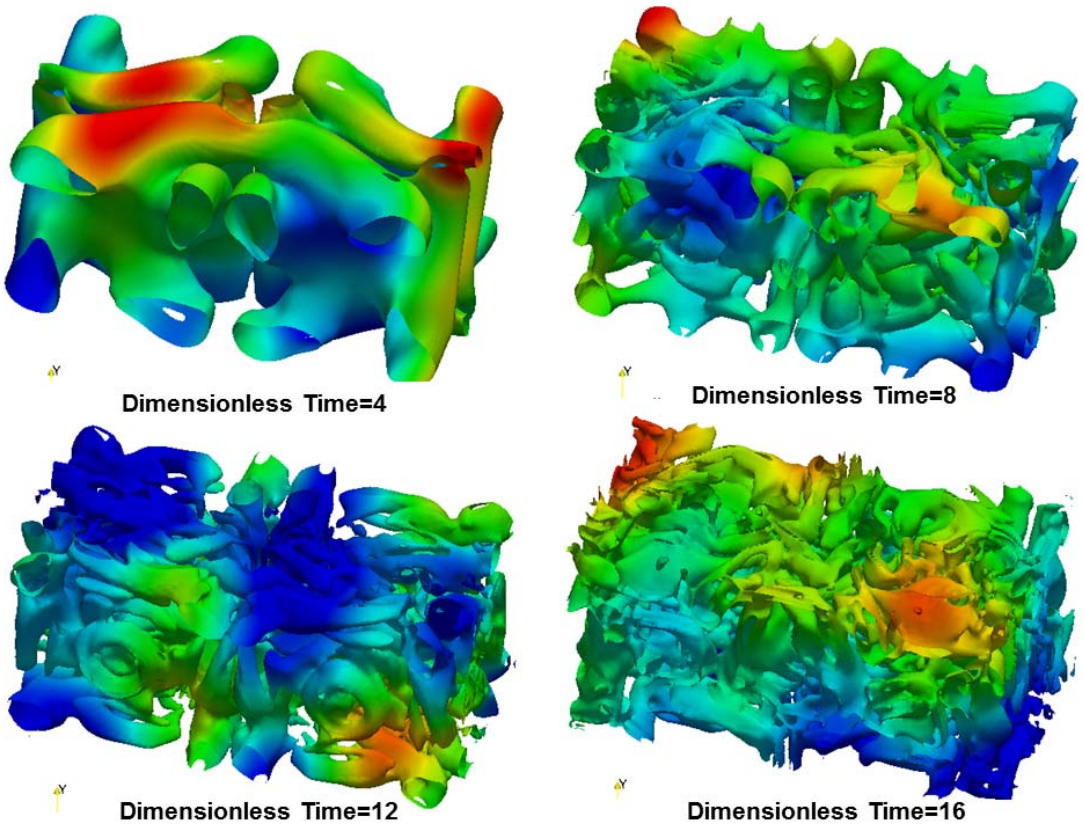

Figure 33. Transition of vortical structure in turbulence at different time instants.

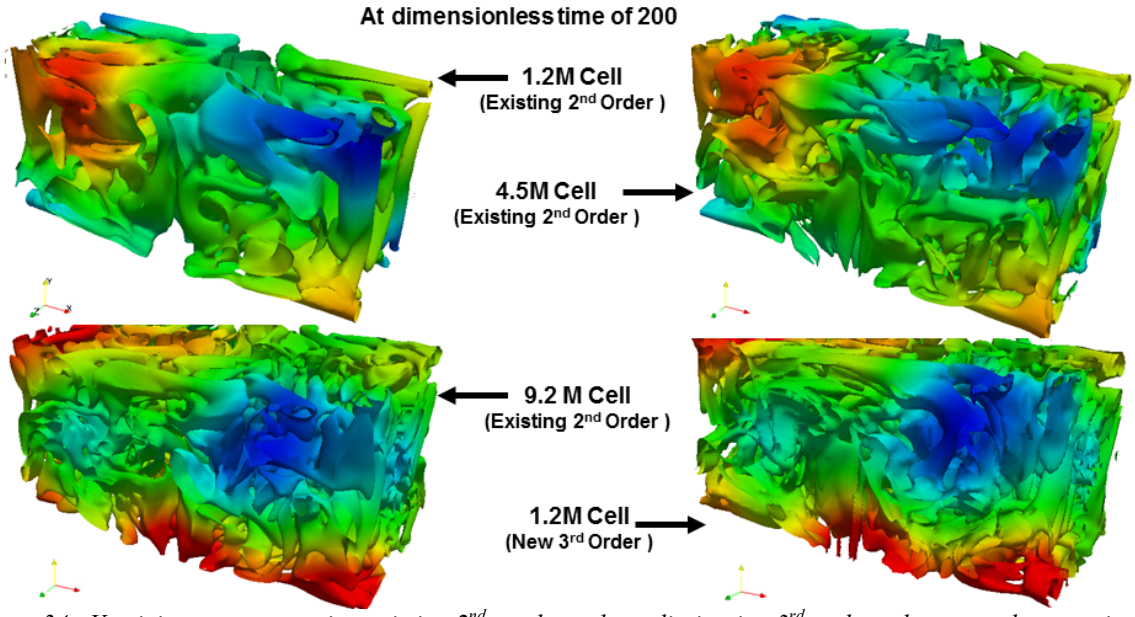

Figure 34. Vorticity structures using existing 2nd- and new low- dissipation 3rd-order schemes at the same instant.

Flow Past A Circular Cylinder at Reynolds Number 3,900

Flow over cylinders has been studied extensively, both numerically and experimentally, in order to gain a better understanding of steady and unsteady flows at various Reynolds numbers. Excellent reviews have been given by Beaudan and Moin [31], Kravchenko and Moin [32], and Ma *et al.* [33]. Studies of the flow phenomena in the cylinder wake are

conducted for many reasons, from direct application in industrial process to validation of numerical schemes. Based on Beaudan and Moin [31], at Reynolds numbers less than about 40, the flow is steady, laminar and symmetrical. Between 40 and 150 the flow remains laminar and is associated with a regular vortex shedding frequency, which increases with Reynolds number. At approximately 180, the flow becomes three-dimensional in the near wake. Between 300 and $2x10^5$ the flow around the surface of the cylinder is laminar, and there is a transition to turbulence in the separated free shear layers. The range between 300 and $2x10^5$ is known as the *subcritical range*. For lower Reynolds numbers in this range, the wake is fully turbulent 30 to 40 diameters downstream of the cylinder, and for the higher Reynolds numbers, the wake is fully turbulent close to the rear of the cylinder. Reynolds numbers between $2x10^5$ and $3.5x10^6$ are classified as a *critical range*.

The flow past circular cylinders at a subcritical Reynolds number of 3,900 is the subject of this study. The flow in this subcritical range features several interesting phenomena, including a laminar boundary layer with unsteady separations and reattachments; flow reversals at the cylinder surface and in the near wake; adverse pressure gradients; transitioning free shear layers; and a turbulent wake with random and periodic Reynolds stresses [31]. The cases have been used to validate LES models by numerous researchers [31-38]. There are data from two separate experiments, which provide measurements of the velocity and Reynolds stresses in the cylinder wake. Lourenco and Shih [34] performed Particle Image Velocimetry (PIV) measurements to obtain mean and phase-averaged data within three diameters downstream, and Ong and Wallace [35] made single sensor measurements of mean velocities and Reynolds stresses in the wake between the closure point of the recirculation bubble and ten diameters aft of the cylinder. The rich physics of the flow and a large amount of experimental data make it an ideal test case for the validation of high-order numerical schemes. Results from the traditional 2^{nd}-order schemes and the present 3^{rd}-order schemes under development are presented and compared to the experimental data of Ong and Wallace [35], and Lourenco and Shih [34] to demonstrate the improved accuracy of high-order schemes and their importance for efficiently resolving complex flows.

Simulation Model

The mesh used for the simulations is shown in Figure 35 and contains 0.3 million hexahedral and 8.8 million prism cells. The mesh consists of 300 points in the circumferential direction, and power law expansion is used in the radial direction away from the cylinder. The smallest cell spacing in the radial direction is $\Delta r_{min}/D = 1.25x10^{-3}$. This spacing is the same as what Beaudan and Moin [31] used for their finest mesh. The spanwise extent of the domain is chosen to be $L_z/D=\pi$ in accordance with many previous studies [31,33,37]. The domain extends 100D in the x-y plane. In accordance with Beaudan and Moin [31], Mittal and Moin [37] and Kravchenko and Moin [32], 48 grid points are used in the spanwise direction.

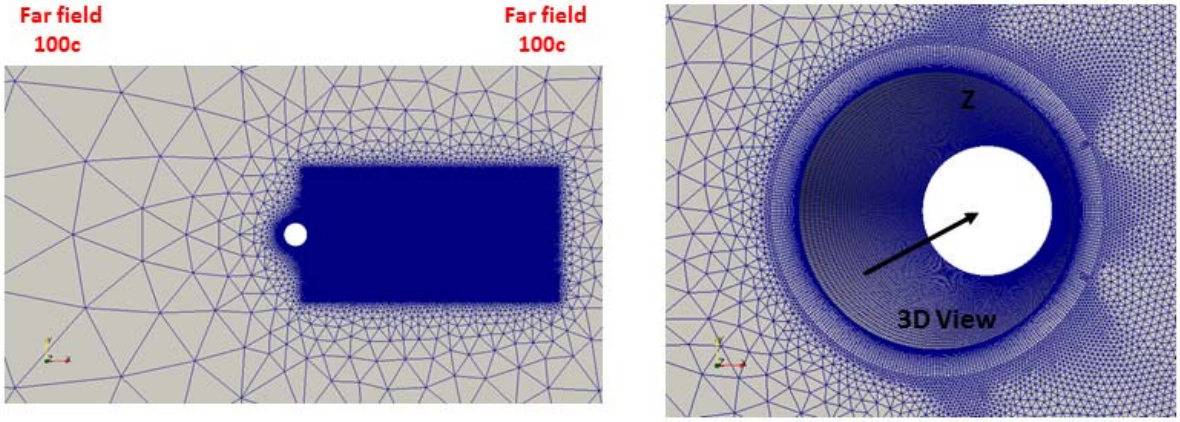

Figure 35. Two different views of computational mesh used for single cylinder simulation.

The outer boundary, which is 100D away from the cylinder, is specified as farfield with a Mach number of 0.1 and zero angle-of-attack. The front and back faces of the mesh in the spanwise direction are given a periodic boundary condition, and a no-slip condition is applied to the cylindrical wall.

The 2^{nd}-order temporal scheme in FUN3D is used for time discretization, with a non-dimensional time step of 0.05. The simulations are first allowed to reach a statistically steady-state before any data is collected, and the data are then averaged in time for statistics.

General Flow Features

The 3D instantaneous Q isosurfaces presented in Figure 36 show a comprehensive picture of the flow structures. The shear layer from the cylinder surface starts to break down into three dimensional vortices and the flow near the trailing edge of the cylinder is essentially turbulent. In the wake of the cylinder, the composition of the small-scale von Karman vortices is visible. As one can see from Figure 36, the 3rd-order upwind scheme is capable of capturing and preserving much smaller vortices.

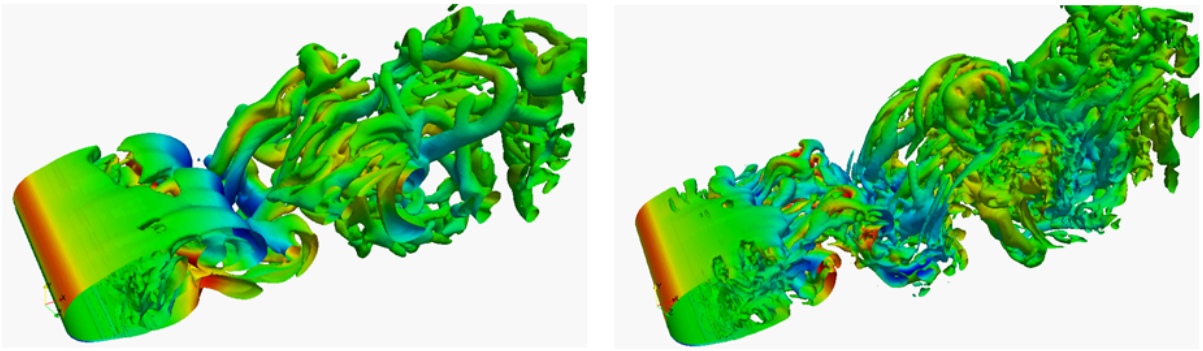

Figure 36. Instantaneous Q iso-surfaces rendered by v velocity component.

Comparison with Experimental Data

Next, we present results from CFD runs using the existing 2nd-order upwind scheme and the new 3rd-order upwind scheme. Comparisons are made with experimental measurements of streamwise velocity at different locations along the streamwise direction. The streamwise data are significantly more reliable than the cross-flow velocity measurements [33]. For example, the experimental uncertainty in the measurements of the streamwise velocity is about 5% while for the cross-flow velocity it is more than 50% according to Beaudan and Moin [31]. As there are no established means by which to define the different regions in the cylinder wake, the convention adopted by Ma *et al*. [33] is employed. Here, the near wake, defined as less than ten diameters aft of the cylinder (i.e. x/D<10), is subdivided into the *very near wake* (x/D<3) where the dynamics of the shear layer dominate, and the *near wake* (3 < x/D < 10).

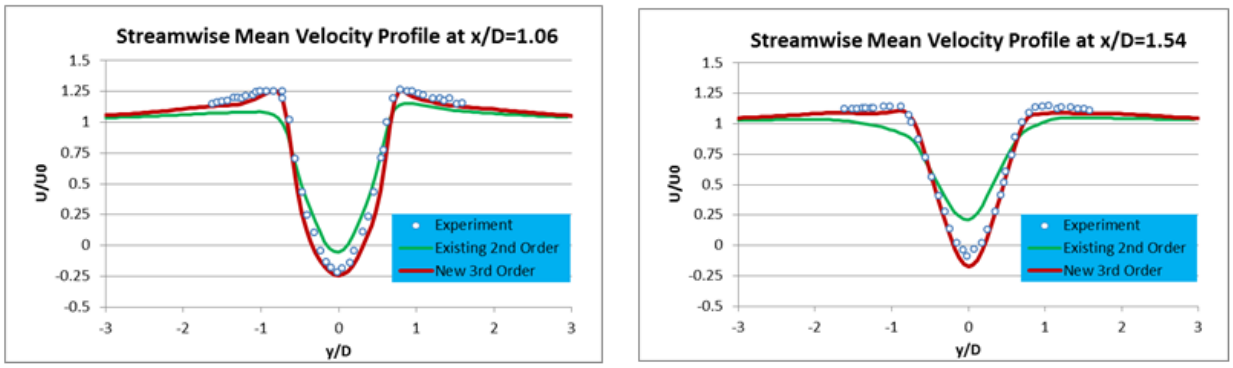

High-order Scheme can resolve smaller vortices and give better agreement with experimental data

Figure 37. Streamwise velocity comparison at x/D=1.06 and 1.54 for different spatial schemes.

PIV experimental data for x/D < 3 at Re=3,900 had been obtained by Lourenco and Shih and were published in Beaudan and Moin [31]. Figure 37 shows the mean streamwise velocity predictions using 2nd-order and 3rd-order schemes at x/D=1.06 and 1.54. One sees that very good agreement is obtained for the 3rd-order upwind scheme, where the time-averaged velocity profile compares well with the V-shaped profile of the data. On the other hand, the results from the 2nd-order upwind are off, while the new 3rd-order scheme has improved the accuracy of the solution.

Figure 38 shows the convergence rate of the 2nd- and 3rd-order schemes. Due to the nature of lower numerical dissipation, the residual from the high-order scheme drops slightly slower than the 2nd-order scheme, which is very much expected. Even with the slowdown, the residuals still drop 4 orders within 10 iterations for both the mass and momentum equations. On the right-hand side of Figure 37, the CPU time required to finish 400 time steps running on 600 processors is presented. The use of the high-order scheme leads to only a 10% increase in CPU time, while, on the other hand, the solution resolution and accuracy have been greatly improved.

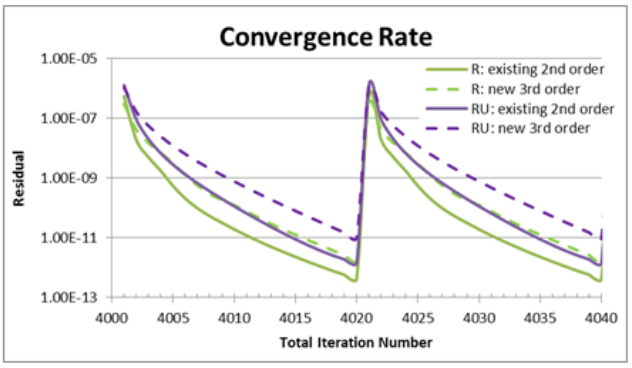

For 400 time steps	CPU Time with 600 processors
Existing 2nd Order Scheme	30 minutes
New 3rd Order Scheme	33 minutes
CPU Overheard	10%

The CPU overhead of the new high-order scheme is about 10%.

Figure 37. Comparison of convergence rate and CPU time between existing 2nd-order and new 3rd-order scheme.

VI. Conclusions

A 3rd-order upwind U-MUSCL type density-based scheme has been derived. The dispersion and dissipation properties of the new scheme are shown to be superior to the existing schemes in FUN3D. A 3rd-order low-dissipation module consistent with the FUN3D code structure has been designed and implemented in FUN3D. Verification studies show that the 3rd-order U-MUSCL scheme can achieve up to 4th-order accuracy on regular grids and up to 3rd-order accuracy on triangular grids. Six problems are identified to evaluate the performance of the new scheme. With just 10% overhead (using same number of iterations per time step), the solution accuracy and associated flow resolution capability can be increased as much as eight times. Considerably better agreement with experimental data when using the new 3rd-order U-MUSCL scheme is demonstrated for transitional flows.

The study had successfully demonstrated the innovation and merit of the current approach to achieve higher order accuracy in the following aspects:

a. *Enabling Higher Accuracy in Existing Unstructured Production CFD Codes*. As many existing unstructured production CFD codes are only up to 2nd-order accurate, the integration of the developed high-order scheme module enables high accuracy in simulating acoustic sources, which is critical for the subsequent propagation. For an existing unstructured production CFD code, in order to capture and preserve an acoustic wave, it typically requires a resolution of at least 16 grid points per wavelength. Our high-order schemes implemented in FUN3D have been shown to reduce the grid point requirement per wavelength so that these high-order schemes will lead to much finer resolutions for high frequency noises. The numerical dispersion and dissipation will also be significantly reduced.

b. *Easy Integration into Existing CFD Codes with Minor Modification*. Unlike the popular DG method, which adds extra DOF into an existing cell, our high-order scheme module uses higher derivatives computed on the existing DOFs. As a result, the higher-order accuracy in the current approach is achieved by adding higher-order correction source terms into the continuity, momentum and energy conservation equations. Only minor modifications to an existing code are needed, and the existing code structure and solution procedure are kept the same. This module can be integrated into any unstructured CFD code, so that many other unstructured production CFD solvers, such as USM3D, Loci/CHEM, in addition to FUN3D, can benefit from this approach.

c. *Efficient Memory Management*. Unlike the DG method, our high-order approach has low memory requirements, and the user can easily switch on the high-order schemes based on the requirements. Only six (6) additional arrays are allocated.

e. *Low-Dissipation and Low Dispersion Errors*. The developed new scheme has superior low dissipation and low dispersion properties compared to the existing 2nd-order scheme in FUN3D. As a result, considerably better agreement

with experimental data has been observed. The high-order scheme enables the same accuracy with a reduced cell account or a better resolution with the same cell count (solving 500M cell problem = solving 1-4B cell problem)

f. *Low-Overhead*. Assessment for many practical problems from inviscid, to laminar, to transition flows indicates that the overhead of the high-order scheme is just 10%, and yet, the spatial resolution can be increased by as much as a factor of eight.

VII. Acknowledgement

This study was supported under a NASA contract number Contract: NNX14CC30P. The authors would like to express their appreciation to the technical monitor Dr. Veer Vatsa of NASA Langley Research Center for his active participation, discussions and guidance.

VIII. References

1. E. Envia, "Emerging Community Noise Reduction Approaches", 3rd AIAA Atmospheric Space Environments Conference, 27-30 June 2011, Honolulu, Hawaii, AIAA-2011-3532.
2. J. J. Berton, E. Envia, and C. L. Burley, "An Analytical Assessment of NASA's N+1 Subsonic Fixed Wing Project Noise Goal", 15th AIAA/CEAS Aeroacoustics Conference (30th AIAA Aeroacoustics Conference), AIAA 2009-3144.
3. Mehdi Khorrami, "From a Roar to a Whisper: Making Modern Aircraft Quieter", Demo for NASA booth at Supercomputing 2012.
4. D. M. Nark, E. Envia, and C. L. Burley, "On Acoustic Source Specification for Rotor-Stator Interaction, Noise Prediction", 16th AIAA/CEAS Aerospace Conference, AIAA-2010-3713.
5. Vatsa, V. and Lockard, D., "Assessment of Hybrid RANS/LES Turbulence Models for Aeroacoustics Applications," AIAA Paper 2010-4001, June 2010.
6. Veer N. Vatsa, Mehdi R. Khorrami, Michael A. Park, David P. Lockard, "Aeroacoustic Simulation of Nose Landing Gear on Adaptive Unstructured Grids with FUN3D", AIAA-2013-2071, May 2013.
7. Veer N. Vatsa, David P. Lockard, Mehdi R. Khorrami, and Jan-Renee Carlson, "Aeroacoustic Simulation of a Nose Landing Gear in an Open Jet Facility using FUN3D", AIAA-2012-2280, June 2012.
8. Veer N. Vatsa, David P. Lockard, and Mehdi R. Khorrami," Application of FUN3D Solver for Aeroacoustics Simulation of a Nose Landing Gear Configuration", AIAA-2011-2820, June 2011.
9. W. Liu, J. W. Kim, X. Zhang, and B. Caruelle, "Simulation of a Generic Two-Wheel Nose Landing Gear Using High-order Finite Difference Schemes", 18th AIAA/CEAS Aeroacoustics Conference (33rd AIAA Aeroacoustics Conference), AIAA 2012-2278. 10Visbal, M. and Gaitonde, D., 1999, "High-Order Accurate Methods for Complex Unsteady Subsonic Flows," AIAA Journal, 37, No. 10, pp. 1231–1239.
10. Visbal, M.R., Gaitonde, D.V., 2002, "On the Use of High-Order Finite-Difference Schemes on Curvilinear and Deforming Meshes," Journal of Computational Physics, 181, pp.155–185.
11. Wang, Z. J. et al., "High-Order CFD Method: Current Status and Perspective", *Int. J. for Numerical Methods in Fluids*, 2013, pp.1-42.
12. Busch, E., et al. "Computational Aeroacoustics with Higher Order Methods", *High Performance Computing in Science and Engineering* '12, 2013, pp 239-253
13. Birkefield, A., Munz, C-D., "Advances in Numerical Aeroacoustics with the Discontinuous Galerkin Solver NoisSol", New Results in Numerical and Experimental Fluid Mechanics VIII Notes on Numerical Fluid Mechanics and Multidisciplinary Design Volume 121, 2013, pp 699-706
14. Duade, et al., "A high-order finite-difference algorithm for direct computation of aerodynamic sound", *Computers & Fluids*, Vol. 61, pp.46-63, 2012.
15. Castonhuay, et al..., 2011, "On the Development of a High-Order, Multi-GPU Enabled, Compressible Viscous Flow Solver for Mixed Unstructured Grids", AIAA-2011-3229.
16. Dumbser, M.,2010, "Arbitrary high-order PnPm schemes on unstructured meshes for the compressible Navier-Stokes equations," *Computers and Fluids*, 39(1), pp. 60–76.
17. Persson Per-Olof, "High-Order Navier-Stokes Simulations Using a Sparse Line-based Discontinuous Galerkin method", AIAA-2012-0456.
18. Ollivier-Gooch, C. and Van Altena, M., 2002, "A high-order-accurate unstructured mesh finite-volume scheme for the advection-diffusion equation," *Journal of Computational Physics*, 181(2), pp. 729–752.
19. Yang, H. Q., Chen, Z. J., Przekwas, A. J., and Dudley, J. D., "High-Order Pressure-based Solver for Aeroacoustic Simulations", 19th AIAA/CEAS Aeroacoustics Conference, 2013, AIAA-2013-2021.
20. Yang, H. Q., Chen, Z. J., and Dudley, J. D., "Development of High-Order Scheme in Unstructured Mesh for Direct

Numerical Simulations", Proceedings of ASME 2013 Fluid Engineering Division Summer Meeting, FEDSM2013-16385, July 07-11, 2013, Incline Village, Nevada, USA.
21. Yang, H. Q., Chen, Z. J., Przekwas, A. J., and Dudley, J. D.,, "A High-order CFD method using successive differentiation", *Journal of Computational Physics*, Vol. 281, pp. 690-707, 2015.
22. FUN3D Web page: http://fun3d.larc.nasa.gov, March 2010.
23. Anderson, W. K. and Bonhaus, D. L., "An Implicit Upwind Algorithm for Computing Turbulent Flows on Unstructured Grids," *Computers and Fluids*, Vol. 23, No. 1, 1994, pp. 1–21.
24. Nielsen, E., Lu, J., Park, M., and Darmofal, D., "An Implicit, Exact Dual Adjoint Solution Method for Turbulent Flows on Unstructured Grids," *Computers and Fluids*, Vol. 33, No. 9, 2003, pp. 1131–1155.
25. Roe, P. L., "Approximate Riemann Solvers, Parameter Vectors, and Difference Schemes", *Journal of Computational Physics*, 250-258, 1987.
26. Barth, T.J. and Frederickson, P.O., "Higher-Order Solution of the Euler Equations on Unstructured Grids Using Quadratic Reconstruction," AIAA-90-0013,1990.
27. Venkatakrishnan, V. and Mavriplis, D.J., "Implicit Solvers for Unstructured Meshes," AIAA-91-1537-CP, 1991.
28. Burg, C. O. E, "Higher Order Variable Extrapolation For Unstructured Finite Volume RANS Flow Solvers", AIAA-2005-4999, 2005.
29. Sherer, S., "Scattering of sound from axisymmetric sources by multiple circular cylinders", *J. Acoust. Soc. Am*. 115 (2), 2004, 488-496.
30. Brachet, M. E., "Direct Numerical Simulation of Three-Dimensional Turbulence in Taylor-Green Vortex", *Fluid Dynamic Research*, 8, 1999 1-8
31. Beaudan, P., Moin, P., "Numerical experiments on the flow past a circular cylinder at sub-critical Reynolds number", In Tech. Rep. TF-62, Dept. Mech. Engng, Stanford University, 1994.
32. Kravchenko, A. G., Moin, P. "Numerical studies of flow over a circular cylinder at ReD = 3900", *Phys. Fluids*, 12, 2000 403-417.
33. Ma, X., Karamanos, G., Karniadakis, G., "Dynamics and low-dimensionality of a turbulent near wake", *J. Fluid Mech*., 410, 2000 29-65.
34. Lourenco, L.M., Shih, C., "Characteristics of the plane turbulent near wake of a circular cylinder". A particle image velocimetry study. Reported in [15].
35. Ong, L., Wallace, J., "The velocity field of the turbulent very near wake of a circular cylinder", *Exp. Fluids*, 20 1996 441-453.
36. Young, M., Ooi, A.,"Comparative assessment of LES and RANS for flow over a cylinder at a Reynolds number of 3900", Proceedings of the Sixteenth Australasian Fluid Mechanics Conference, The University of Queensland, 2007 1063-1070.
37. Mittal, R., P. Moin, P., "Large-eddy simulation of flow past a circular cylinder, APS Bulletin", 41(9), 1996 49th DFD Meeting.
38. Franke, J., Frank, W., "Large eddy simulation of the flow past a circular cylinder at ReD = 3900", *J. Wind Eng. Ind. Aerod*., 90, 2002 1191-1206.